Dual targeting of PDPK1 and BRAF V600E is synthetically lethal

Tejinder Pal Khaket[1*], Chandrayee Ghosh[1], Zhongyue Yang[1], Myriem Boufraqech[3], Jiangnan Hu[1], Eden D. Alamaw[4], Thorkell Andresson[6], Maura O'Neill[6], Ya-Qin Zhang[7], Min Shen[7], Bereketeab Haileselassie[8], Electron Kebebew[1,2**]

[1]Department of Surgery, Stanford University, Stanford, CA, USA

[2]Stanford Cancer Institute, Stanford University, Stanford, CA, USA

[3]Surgical Oncology Branch, Center for Cancer Research, National Cancer Institute, NIH, MD, USA

[4]Department of Comparative Medicine, Stanford University, CA, USA

[5]Department of Comparative Medicine, Veterinary Service Center, Stanford University, Stanford, CA, USA.

[6]Protein and Metabolite Characterization Core, Cancer Research Technology Program, Frederick National Laboratory for Cancer Research, Frederick, MD, USA

[7]National Center for Advancing Translational Sciences, National Institute of Health, Bethesda, MD, USA

[8]Lucile Packard Children's Hospital, Stanford University, CA, United States

Corresponding Authors:

*Tejinder Pal Khaket, tpkhaket@stanford.edu

** Electron Kebebew, kebebew@stanford.edu

ABSTRACT

PDPK1 functions downstream of PI3K and is essential for activating AKT and other AGC kinases. Although PDPK1 has a central role in the PI3K/AKT/mTOR signaling pathway, there has been limited evaluation of it as a target for cancer therapy. Anaplastic thyroid cancer (ATC) has one of the highest mortality rates of all human malignancies. Although combined BRAF and MEK inhibition in BRAF V600E mutant ATC (present in 45% of cases) results in response, resistance is common, and there is no curative treatment for ATC. The majority (up to 95.8%) of ATC cases have activation in the PI3K/AKT/mTOR and RAS/RAF/MEK/MAPK pathways due to genetic alterations involved in these pathways. In this study, we investigated PDPK1 as a therapeutic target for ATC. We used in vitro, ex vivo, and in vivo ATC models to evaluate the effect of targeting PDPK1 (BX795) alone and in combination with BRAF V600E inhibition (dabrafenib), and the mechanism of action that resulted in ATC cell death. BX795 monotherapy significantly reduced ATC cell proliferation, invasion, colony formation, and spheroid size. Combination BX795 and dabrafenib treatment had strong synergistic anticancer activity in BRAF V600E-mutant ATC models and led to simultaneous and sustained suppression of PDPK1/AKT and MAPK signaling, preventing the compensatory pathway reactivation observed with single-agent treatment. Mechanistically, combined inhibition induced pronounced oxidative stress, DNA damage, and G2-phase cell-cycle arrest, accompanied by mitochondrial dysfunction and robust activation of apoptosis in ATC cells. These effects resulted in marked tumor regression in in vitro, ex vivo, and in vivo ATC models. Our findings identify PDPK1 as a critical therapeutic vulnerability in ATC. Co-targeting PDPK1 and BRAF V600E produces potent synergistic anticancer activity by shutting down convergent oncogenic signaling pathways and amplifying apoptotic stress responses. These data support PDPK1 inhibition alone and in combination with BRAF blockade as a promising therapeutic strategy in BRAF V600E-mutant cancers.

52 **Keywords:** Anaplastic thyroid cancer; PDPK1, *BRAF* V600E mutation, BX795, cell cycle arrest,
53 synergism
54

55 **INTRODUCTION**

56 Anaplastic thyroid cancer (ATC) is a rare (incidence of 1–2 cases per million people) and
57 lethal cancer. Although ATC accounts for 1%–2% of all thyroid cancer cases, it is responsible for
58 two-thirds of all thyroid cancer deaths and has a median survival time of only 6 months (1–3).
59 Recent advances in the understanding of genetic alterations in ATC have revealed that the majority
60 (up to 95.8%) of ATC cases have activation in the PI3K/AKT/mTOR and MAPK/ERK (also
61 known as RAS/RAF/MEK/MAPK) pathways due to genomic alterations (driver mutations and
62 genomic gains/losses) involved in these pathways (4,5). Targeting driver mutations, such as *BRAF*
63 V600E (present in 45% of ATC cases), in mutant ATC elicits a response in some cases, but
64 development of resistance to treatment and treatment-related toxicity that results in treatment
65 stoppage are common (3,6–10). Thus, there is an urgent need to develop new therapeutic strategies
66 for ATC that elicit a significant and durable response and thereby extend patient survival.

67 Although inhibition of the MAPK/ERK pathway in *BRAF* V600E–mutant ATC, using
68 BRAF and MEK inhibitors, is effective, compensatory upregulation and acquired mutations in the
69 PI3K/AKT/mTOR pathway commonly undermine this strategy, leading to therapeutic resistance
70 (11–16). Within the PI3K/AKT/mTOR signaling pathway, 3-phosphoinositide-dependent kinase 1
71 (PDPK1 or PDK1) functions downstream of PI3K and is essential for activating AKT and other
72 AGC kinases (17,18). Although PDPK1 has a central role in the PI3K/AKT/mTOR signaling
73 pathway, there has been limited investigation of it as a target for cancer therapy (18). Gene
74 mutations that lead to activation of the PI3K/AKT/mTOR pathway are common in ATC and occur
75 in genes upstream of PDPK1. However, direct evidence of PDPK1 phosphorylation in ATC has
76 not yet been reported, representing an important knowledge gap. Phosphorylation of PDPK1 at
77 Ser241 is essential for its activity in phosphorylating AKT at Thr308 and its association with
78 cancer initiation and progression (19). PDPK1 overexpression drives cancer initiation and

79 progression in a range of malignancies, and is associated with more aggressive tumors (20–38).
80 PDPK1 is also overexpressed in thyroid cancer, where higher levels are associated with more
81 advanced disease and ATC (39). Accumulating evidence indicates that PDPK1-mediated AKT
82 activation plays a central role in cancer initiation and progression (40–44).

83 Investigating PDPK1 activation in ATC could provide both mechanistic insight and define
84 the potential of targeting it for ATC therapy and other cancers with activation in the
85 PI3K/AKT/mTOR pathway. Therefore, we evaluated the anticancer activity of targeting PDPK1
86 using *in vitro*, *ex vivo*, and *in vivo* models in ATC with and without *BRAF* V600E inhibition.

87

88 **MATERIALS AND METHODS**

89 **Materials**

90 The materials used in this study are listed in Tables S1 (list of antibodies), S2 (list of
91 chemicals), and S3 (cell lines and their mutation status).

92

93 **Cell lines and culture conditions**

94 The homozygous mutated *BRAF* V600E 8505C, FTC133 (homozygous mutated *PTEN*),
95 and FTC236 (homozygous mutated *PTEN*) human thyroid cancer cell lines were purchased from
96 the European Collection of Cell Culture (Salisbury, UK). The heterozygous mutated *BRAF* V600E
97 human ATC cell line SW1736 and the *BRAF* wild type ATC cell line C643 (heterozygous mutated
98 *PTEN*) were purchased from Cell Lines Service GmbH (Eppelheim, Germany). The THJ-11T
99 (*KRAS* mutant), THJ-29T, and THJ-16T (*PIK3CA* mutant) ATC cell lines were a kind gift from Dr.
100 John A. Copland III (Mayo Clinic, Jacksonville, FL). The BCPAP (homozygous mutated *BRAF*
101 V600E) cell line was purchased from Leibniz Institute DSMZ (Lower Saxony, Germany). The
102 TPC1 (*RET/PTC1* rearrangement) cell line was purchased from Sigma-Aldrich, Inc. (St. Louis,

103 MO, USA). Details of cell line–specific mutations are provided in Table S3. The HEK293 cell line
104 was purchased from American Type Culture Collection (Manassas, VA, USA). All cells were
105 cultured in Dulbecco's Modified Eagle's Medium (DMEM, which contains 4,500 mg/L of D-
106 glucose, 2 mmol/L of L-glutamine, and 110 mg/L of sodium pyruvate) supplemented with 10%
107 fetal bovine serum (FBS), and antibiotics (penicillin and streptomycin at 10,000 U/mL) at 37 °C
108 and 5% CO_2. Two patient-derived *BRAF* V600E–mutant ATC cell lines—ATC-01, derived from a
109 treatment-naïve patient's primary *BRAF* V600E–mutant tumor, and ATC-02, derived from a *BRAF*
110 V600E–mutant residual tumor following combination therapy with dabrafenib (Dab) and
111 trametinib (*BRAF* and MEK inhibitors, respectively)—were maintained in DMEM:F12
112 supplemented with 15% FBS and antibiotics (penicillin and streptomycin at 10,000 U/mL) at 37
113 °C and 5% CO_2 in a humidified incubator.
114
115 **Quantitative high-throughput screening**
116 Quantitative high-throughput screening was used to screen the 8505C, THJ-11T, and THJ-
117 16T ATC cell lines based on the National Center for Advancing Translational Sciences (NCATS)
118 Pharmaceutical Collection (NPC) and the Mechanism Interrogation PlatE (MIPE) library with
119 4,991 small-molecule drugs and investigational compounds. Cell viability was measured using a
120 luciferase-coupled adenosine triphosphate (ATP) quantitation assay (CellTiter-Glo®, Promega,
121 Madison, WI, USA). To identify the optimal PDPK1 inhibitor, drug response data of PDPK1
122 inhibitors (BX-912, DTXSID90678515, OSU-03012, GSK-2334470, and BX795) present in the
123 high-throughput screening library were analyzed.
124
125 **Cell proliferation assay**

126 Cells were seeded in 96-well black plates (Greiner Bio-One, Kremsmünster, Austria) at a
127 density of 1.5×10^3 cells per well. After 24 h, cells were treated in triplicate with the indicated
128 concentrations of Dab, BX795, and other small molecules for 48 h at 37 °C and 5% CO_2 in a
129 humidified incubator. Dimethyl sulfoxide (DMSO) was used as a vehicle control. CyQUANT cell
130 proliferation assays were performed according to the manufacturer's instructions, and the results
131 were analyzed using a SpectraMax i3x Multi-Mode Microplate Reader (Molecular Devices, San
132 Jose, CA, USA) at an excitation wavelength of 480 nm and an emission wavelength of 530 nm.
133 The relative fold change was measured as compared to the control. Statistical analyses were
134 performed using GraphPad Prism version 10 (GraphPad Software Inc., San Diego, CA, USA).
135

136 **Calculation of combination drug activity**

137 After treating ATC cells with various concentrations of DMSO (control), BX795, Dab, or
138 their combination (BX795 + Dab) for 48 h, cell proliferation was measured. Then, drug responses
139 were analyzed using the CompuSyn software (Version 1.0) based on the Chou–Talalay method
140 (45) to determine synergy, additivity, or antagonism. The combination index (CI) was calculated,
141 where CI < 1 indicates synergy, CI = 1 indicates an additive effect, and CI > 1 indicates
142 antagonism. The values were derived from drug combinations applied at non-constant ratios.
143

144 **Clonogenic assay**

145 Cells (1×10^3 cells/well) were seeded in 12-well plates and allowed to adhere overnight.
146 Then, cells were treated in triplicate with DMSO (control), BX795 (2.5 μM), Dab (2.5 μM), or
147 their combination (BX795 + Dab) for 48 h, after which time the medium was replaced with fresh
148 complete DMEM, and colonies were allowed to form for up to 8–12 days. Colonies were fixed
149 with 4% buffered paraformaldehyde for 10 min at room temperature, washed with phosphate-

150 buffered saline (PBS), and then stained with 0.5% crystal violet for 30 min at room temperature
151 with continuous shaking. Finally, stained colonies were washed with water, and the ImageJ
152 software (National Institutes of Health, Bethesda, MD, USA) was used for quantification.
153 GraphPad Prism version 10 was used for statistical analysis.
154
155 **Migration assay**
156 A wound-healing assay was performed to analyze cellular migration. In brief, a scratch
157 (wound) was generated using a sterile pipette tip, and cells were washed with PBS; treated in
158 triplicate with DMSO (control), BX795 (2.5 μM), Dab (2.5 μM), or their combination (BX795 +
159 Dab); and incubated in DMEM supplemented with 2% FBS for 16–24 h. Finally, wound-healing
160 was measured using ImageJ. The results are presented as the relative change in cellular migration
161 compared to the control.
162
163 **Spheroid formation assay**
164 Mutant *BRAF* V600E ATC cells (8505C, SW1736, ATC01, and ATC02) were seeded in
165 round bottom, ultra-low attachment 96-well plates (1.5×10^3/well) using 3D Tumorsphere Medium
166 XF (PromoCell, Heidelberg, Germany) and placed in a humidified incubator at 37 °C with 5%
167 CO_2 for spheroid formation. After 72 h, spheroids were treated with DMSO (control), BX795 (2.5
168 μM), Dab (2.5 μM), or their combination (BX795 + Dab), and monitored over 7 days. Images of
169 each spheroid were acquired after 0 and 8 days of treatment. The size was quantified using ImageJ.
170 The data are presented as the relative change in spheroid size compared to the control.
171
172 **Quantitative proteomic and phosphoproteomic analysis**
173 ***Sample preparation and tandem mass tag (TMT) labeling***

174 Mutant BRAF V600E ATC cell lines were treated with DMSO (control), BX795 (2.5 μM),
175 Dab (2.5 μM), or their combination (BX795 + Dab) for 48 h. Cell pellets were resuspended in 200
176 μL of EasyPep™ lysis buffer (Thermo Fisher Scientific, Waltham, MA, USA) supplemented with
177 nuclease (1 μL), protease inhibitors, and PhosSTOP (Sigma-Aldrich, Inc., St. Louis, MO, USA).
178 Protein concentrations were determined with the BCA protein assay, and 100 μg of protein per
179 sample was mixed with 50 μL of reduction reagent and 50 μL of alkylation reagent. Samples were
180 digested overnight at 37 °C with 6 μg of trypsin/Lys-C at 750 rpm. The following day, 200 μg of
181 the TMTpro reagent (Thermo Scientific) was added, and samples were incubated for 1 h at 25 °C.
182 Labeling reactions were quenched with 5% hydroxylamine and 20% formic acid (50 μL, 10 min).
183 TMT-labeled peptides were combined, cleaned using the EasyPep™ Maxi Kit, and dried in a
184 vacuum concentrator.
185
186 ***Phosphopeptide enrichment***
187 Sequential phosphopeptide enrichment was performed using the High-Select TiO_2 and Fe-
188 NTA IMAC kits (Thermo Fisher Scientific) following the manufacturer's protocols. Peptides were
189 first enriched by TiO_2; the TiO_2 flow-through and wash fractions were collected, dried, and
190 subjected to a second enrichment using immobilize metal affinity chromatography (IMAC). Eluted
191 phosphopeptides from both steps were combined, dried, and reserved for liquid chromatography–
192 tandem mass spectrometry (LC–MS/MS) analysis. IMAC flow-through and wash fractions were
193 saved for high-pH fractionation.
194
195 ***High-pH reverse-phase fractionation***
196 IMAC flow-through peptides were resuspended in 100 μL of LC/MS-grade water, and 85
197 μL was fractionated by high-pH reverse-phase ultra-performance liquid chromatography (UPLC)

198 (ACQUITY, Waters, Milford, MA). Peptides were separated on a 150 mm × 3.0 mm XBridge
199 Peptide BEH C18 column (2.5 µm) at 0.35 mL/min. After a 5-min wash with mobile phase A (10
200 mM ammonium formate, pH 9.4), peptides were eluted using a gradient of 10%–50% mobile phase
201 B (10 mM ammonium formate/90% acetonitrile, pH 9.6; 5–60 min), followed by 50%–75% B
202 (60–70 min). Fractions were collected every minute, generating 60 fractions, which were pooled
203 into 12 final fractions, dried, and stored at −80 °C until analysis.
204
205 ***LC–MS/MS analysis***
206 Dried fractions were resuspended in 0.1% formic acid, and 5 µL was injected into a Dionex
207 UltiMate 3000 RSLC system coupled to an Orbitrap Eclipse mass spectrometer (Thermo Fisher
208 Scientific) equipped with FAIMS and an EasySpray source. Chromatographic separation was
209 performed at 300 µL/min using solvent A (0.1% formic acid) and solvent B (80% acetonitrile/0.1%
210 formic acid) with the following gradient: 5%–7% B (1 min), 7%–30% B (83 min), 30–59% B (25
211 min), 50%–95% B (4 min), 95% B (7 min), and re-equilibration at 5% B (17 min). The mass
212 spectrometer was operated in TopSpeed mode using four FAIMS compensation voltages (−45,
213 −55, −65, and −75). MS1 scans were acquired in the Orbitrap at 120,000 resolutions with an
214 automatic gain control (AGC) target of 4×10^5 and a maximum injection time of 50 ms over 375–
215 1600 m/z. MS2 spectra were acquired using the TurboTMT method at 15,000 resolutions (an AGC
216 target of 5×10^4, an isolation window of 1.6 m/z, a higher-energy collisional dissociation [HCD]
217 of 30%, and a minimum intensity of 2.5×10^4). Monoisotopic precursor selection, Easy-IC internal
218 calibration, and advanced peak determination were enabled. For phosphopeptide runs, two FAIMS
219 methods were used, each containing four compensation voltages (CVs) (a cycle time of 0.75 s per
220 CV; 3 s total): Method 1 (−45, −55, −65, and −75) and Method 2 (−50, −60, −70, and −80).
221

222 ***Database searching and quantification***

223 Raw files were processed in Proteome Discoverer using the Sequest HT node. Spectra were
224 searched against the UniProt human database with full trypsin specificity, allowing up to two
225 missed cleavages and a minimum peptide length of six residues. Tolerance was set to 10 ppm for
226 MS1 and 0.02 Da for MS2. Carbamidomethylation of cysteine, TMTpro labeling of lysine and
227 peptide N-termini, and phosphorylation of serine/threonine/tyrosine were specified as static or
228 variable modifications as appropriate. Methionine oxidation was included as a variable
229 modification. PSM-, peptide-, and protein-level false-discovery rates (FDRs) were controlled with
230 Percolator. Reporter ion intensities were quantified using the Reporter Ion Quantifier node and
231 normalized to the total peptide abundance per channel.

232

233 ***Proteomic and phosphoproteomic data analysis and pathway enrichment***

234 All proteomic and phosphoproteomic analyses were performed in R version 4.2 using a
235 reproducible workflow. The data were imported with readr (v2.1.4) and processed using dplyr
236 (v1.1.4) and tidyr (v1.3.0), with removal of contaminants and low-confidence entries. Phosphosite-
237 level specificity was preserved by generating unique feature identifiers combining gene symbol
238 and phosphorylation site annotation (*Gene|site_label*), and numeric columns were explicitly
239 coerced to the numeric format. Differential abundance or phosphorylation was assessed for each
240 treatment condition (BX795, Dab, and their combination) relative to the control, yielding $\log_2$ fold
241 changes ($\log_2$FCs) and associated p-values, with multiple testing correction applied using the
242 Benjamini–Hochberg method. Volcano plots ($\log_2$FC versus $-\log_{10}$(p-value)) and Venn diagrams
243 of significantly regulated features were generated using ggplot2 (v3.4.4), ggrepel (v0.9.4), and
244 ggVennDiagram (v1.2.2). Gene set enrichment analysis (GSEA) was performed with fgsea
245 (v1.28.0) using a signed ranking metric (sign($\log_2$FC) × $-\log_{10}$(p-value)) and curated Kyoto

246 Encyclopedia of Genes and Genomes (KEGG) and MSigDB Hallmark gene sets, reporting
247 normalized enrichment scores (NESs) with FDR-adjusted q-values. In addition, enrichment
248 heatmaps were produced with pheatmap (v1.0.12). All figures were exported at publication-quality
249 resolution.
250
251 **Cell cycle analysis**
252 Mutant *BRAF* V600E ATC cells (8505C and SW1736) were treated overnight with DMSO
253 (control), BX795 (2.5 μM), Dab (2.5 μM), or their combination (BX795 + Dab). Then, cells were
254 trypsinized and fixed using pre-chilled 70% ethanol, followed by overnight incubation at –80 °C.
255 The next day, cells were thawed and centrifuged at 1500 rpm for 5 min, washed with PBS, and
256 stained with FxCycle™ PI/RNase staining solution (Thermo Fisher Scientific) for 30 min at room
257 temperature. After incubation, the cell cycle and DNA content (2N or 4N) were analyzed with a
258 BD Accuri C6 Plus flow cytometer (BD Biosciences, San Jose, CA, USA). Experiments were
259 performed in triplicate, and the results are reported compared to the control.
260
261 **Apoptosis assay**
262 Apoptotic cells were identified using the Annexin V/Dead Cell Apoptosis Kit (BD
263 Biosciences) as per the manufacturer's protocol. Briefly, mutated *BRAF* V600E ATC cells (8505C
264 and SW1736) were treated for 48 h with DMSO (control), BX795 (2.5 μM), Dab (2.5 μM), or
265 their combination (BX795 + Dab). Then, cells were harvested, trypsinized, and washed with ice-
266 cold PBS. The single-cell suspension was resuspended in 100 μL of 1× annexin-binding buffer
267 with 5 μL each of Annexin V and propidium iodide (PI), followed by incubation for 20 min at
268 room temperature. Annexin V/PI-stained cells were measured using a BD Accuri C6 Plus flow
269 cytometer (BD Biosciences). The relative fold change was determined compared to the control.

270

271 **Reactive oxygen species (ROS) measurement**

272 Cellular ROS were measured using DCHFDA staining. Mutant *BRAF* V600E ATC cells
273 (8505C and SW1736) were treated 24h with DMSO (control), BX795 (2.5 μM), Dab (2.5 μM), or
274 their combination (BX795 + Dab). After treatment, cells were trypsinized, washed with PBS, and
275 stained with DCHFDA (5 μM) for 30 min in the dark. After incubation, DCHFD fluorescence was
276 measured using a BD Accuri C6 Plus flow cytometer (BD Biosciences). The results are presented
277 as relative fold change compared to the control.

278 Mitochondrial ROS production was measured using Mito-SOX™ Red mitochondrial
279 superoxide indicator. After treatment overnight, cells were harvested, trypsinized, washed with
280 PBS, and stained with 2.5 μM Mito-SOX Red for 20 min at 37 °C. Mito-SOX™ fluorescence was
281 measured using a BD Accuri C6 Plus flow cytometer (BD Biosciences). The results are presented
282 as relative fold change compared to the control.

283

284 **Mitochondrial content measurement**

285 Mitochondria were visualized using MitoTracker Green FM (Thermo Fisher Scientific),
286 which labels mitochondria independently of the membrane potential. Mutant *BRAF* V600E ATC
287 cells (8505C and SW1736) were seeded onto sterile coverslips in 12-well plates; allowed to adhere
288 overnight; and treated with DMSO (control), BX795 (2.5 μM), Dab (2.5 μM), or their combination
289 (BX795 + Dab). After treatment, cells were stained with 50 nM MitoTracker Green for 30 min at
290 37 °C in the dark. Then, cells were washed with PBS, and live cell fluorescence imaging was
291 acquired using a SP8 confocal microscope (Leica, Wetzlar, Germany) at 400× magnification under
292 identical acquisition settings for all samples at multiple sites on each slide. Fluorescence intensity
293 was quantified using ImageJ.

294 In addition, single-cell suspensions of treated cells were stained in triplicate with 50 nM
295 MitoTracker Green FM for 30 min at 37 °C in the dark. Cellular fluorescence was measured using
296 a BD Accuri C6 Plus flow cytometer (BD Biosciences). The results are presented as the relative
297 fold change compared to the control.
298
299 **Measurement of mitochondrial transmembrane potential**
300 The mitochondrial membrane potential was analyzed by using the Image-iT™ TMRM
301 Reagent (Thermo Fisher Scientific). Mutant *BRAF* V600E ATC cells (8505C and SW1736) were
302 treated overnight in triplicate with DMSO (control), BX795 (2.5 μM), Dab (2.5 μM), or their
303 combination (BX795 + Dab). After treatment, cells were trypsinized, and single-cell suspensions
304 were stained with TMRM (100 nM) for 30 min at 37 °C in the dark. Following treatment, cells
305 were washed and resuspended in ice-cold PBS. Fluorescence was measured using a BD Accuri C6
306 Plus flow cytometer (BD Biosciences). The results are presented as the relative fold change
307 compared to the control.
308 Mitochondrial depolarization was measured with the potentiometric dye JC-1. After
309 treatment 24h with DMSO (control), BX795 (2.5 μM), Dab (2.5 μM), or their combination
310 (BX795 + Dab), mutant *BRAF* V600E ATC cells (8505C and SW1736) were stained with JC-1
311 (2 μM) for 30 min at 37 °C in the dark, washed, and resuspended in ice-cold PBS. Red and green
312 fluorescence was measured using a BD Accuri C6 plus flow cytometer (BD Biosciences). The
313 results are presented as the relative ratio of red versus green fluorescence compared to the control.
314
315 **Measurement of the oxygen consumption rate (OCR)**
316 The OCR was measured using a Seahorse XFe24 Extracellular Flux Analyzer (Seahorse
317 Bioscience, Santa Clara, CA). Mutant *BRAF* V600E ATC cells (8505C and SW1736) were seeded

318 evenly in XF24 microplates; allowed to adhere for 24 h; and then treated for an additional 24 h
319 with DMSO (control), BX795 (2.5 μM), Dab (2.5 μM), or their combination (BX795 + Dab).
320 Measurements were performed in XF assay medium containing 1 mM sodium pyruvate, 2 mM
321 glutamine, and 10 mM glucose under basal conditions. After washing with assay medium, cells
322 were incubated at 37 °C in a non-CO_2 incubator for 30 min. The baseline OCR was recorded,
323 followed by sequential injections of oligomycin (1 μM, an ATP synthase inhibitor), FCCP (4 μM,
324 a mitochondrial uncoupler), rotenone (1 μM, a complex I inhibitor), and antimycin A (1 μM, a
325 complex III inhibitor) using Seahorse XFe24 Extracellular Flux Analyzer (Seahorse Bioscience).
326 Mitochondrial function parameters were calculated as follows: basal OCR = baseline OCR − OCR
327 after rotenone/antimycin A; ATP-linked OCR = basal OCR − OCR after oligomycin; maximal
328 respiration = OCR after FCCP − OCR after rotenone/antimycin A. The assay involved 3 min of
329 mixing, 3 min of waiting, and 3 min of measurement. The data were normalized to the total protein
330 content and are presented as the mean ± standard deviation (SD).
331
332 **Western blot analysis**
333 Lysates from mutant *BRAF* V600E ATC cells (8505C and SW1736) were prepared in
334 radioimmunoprecipitation assay (RIPA) buffer supplemented with phosphatase and protease
335 inhibitors. Protein concentrations were determined using the Pierce™ BCA Protein Assay Kit
336 (Thermo Fisher Scientific). Equal amounts of protein were separated by electrophoresis on 4%–
337 15% precast sodium dodecyl sulfate–polyacrylamide gel electrophoresis (SDS-PAGE) gels and
338 transferred to nitrocellulose membranes. Membranes were incubated overnight at 4 °C with
339 primary antibodies (Table S1), followed by horseradish peroxidase (HRP)-conjugated secondary
340 antibodies (Table S1). Protein bands were visualized using enhanced chemiluminescence (ECL)

341 and imaged with a Bio-Rad ChemiDoc™ MP Imaging System (Bio-Rad, Hercules, CA, USA).
342 Band intensities were quantified using ImageJ.
343
344 **Immunofluorescence**
345 Mutant *BRAF* V600E ATC cells (8505C and SW1736) were treated overnight with DMSO
346 (control), BX795 (2.5 μM), Dab (2.5 μM), or their combination (BX795 + Dab). Then, cells were
347 washed with PBS, fixed 3 × 15 min using chilled methanol, washed 3 × 5 min with PBS,
348 permeabilized by PBS containing 0.2%Triton X-100, and finally washed three times with PBS.
349 Cells were incubated with 1% bovine serum albumin containing 0.02% Tween 20 for 30 min at
350 room temperature (to block nonspecific protein binding), followed by incubation overnight with
351 the pH_2AX primary antibody (Table S1) at 4 °C. The next day, cells were washed three times with
352 PBS containing 0.02% Tween 20 (PBST) and incubated with fluorescently labelled secondary
353 antibodies (Table S1) for 2 h at room temperature. Finally, cells were washed with PBST and
354 counterstained with mounting media containing DAPI. Labelled proteins were observed using an
355 SP8 confocal microscope (Leica) at 400× magnification. The number of H2AX foci among 25
356 cells was counted for each treatment. The results are presented as the number of foci (mean ±
357 standard error of the mean [SEM]).
358
359 **Orthotopic ATC xenograft model**
360 For the orthotopic ATC model, 1×10^6 8505C-Luc2 cells (Luc2 denotes cells with stable
361 expression of a luciferase reporter) were implanted into the thyroid gland of male and female *NOD*
362 *Cg-Prkdcs^{cid} Il2rg^{tm1Wjl}/SzJ* mice. All animal procedures were approved by the Stanford
363 Administrative Panel on Laboratory Animal Care (APLAC; Protocol #34767) and conducted in
364 accordance with institutional and federal guidelines. Tumor luminescence was measured using the

365 Lago (Spectral Instruments Imaging, Tucson, AZ, USA) after intraperitoneal luciferin injection
366 (150 mg/kg). One week after orthotopic implantation, 10 mice (5 males and 5 females) were
367 randomized into four treatment groups: vehicle control (CM-cellulose), BX795 (100 mg/kg), Dab
368 (15 mg/kg), and BX795 (100 mg/kg) + Dab (15 mg/kg). BX795 and Dab were solubilized in
369 methyl cellulose (0.5% in double-distilled water) with sonication (Picoruptor, Diagenode Inc,
370 Devville, NJ, USA) at 4 °C. They were administered orally 5 days/week for 2 weeks with
371 continuous monitoring for toxicity. Mice were imaged and weighed weekly. After treatment, all
372 mice were euthanized using CO_2 inhalation. Tumor, lung, and liver samples were collected after
373 euthanasia. Tumor size and weight were recorded, and thyroid tumor, lung, liver, and kidney
374 samples were collected for histopathological evaluation.
375
376 **Statistical analyses**
377 The data are presented as the mean ± SD, with the details for each analysis provided in the
378 figure legends. Note that the *in vivo* results and number of H_2AX foci are presented as the mean ±
379 SEM. All *in vitro* experiments were performed in at least three independent experiments. Analysis
380 of variance (ANOVA) was used to determine the differences between groups. GraphPad Prism
381 version 10 (GraphPad Software, San Diego, CA) was used for all statistical analyses. The level of
382 statistical significance is indicated as follows: ns is nonsignificant; *$p < 0.05$; **$p < 0.01$; ***$p <$
383 0.001; and ****$p < 0.0001$.
384
385 **RESULTS**
386 **Functional dependency on PDPK1 in ATC**
387 To assess PDPK1 as a therapeutic vulnerability in ATC, we integrated DepMap CRISPR
388 Chronos dependency scores with PDPK1 expression across cancer lineages. PDPK1 showed broad

389 essentiality (median Chronos ≈ –0.88), with thyroid cancers clustering among the highly
390 dependent groups, comparable to bowel and pancreatic cancers. Within the thyroid lineage,
391 PDPK1 transcript levels were similar across medullary, well-differentiated, and anaplastic thyroid
392 cancer cell lines (Fig. S1A–B). In contrast, functional dependency analysis revealed marked
393 PDPK1 dependence in both ATC (Chronos –0.65 to –1.15; median –0.84) and WDTC (–0.606 to
394 –1.15; median –0.98) models (Fig. S1C). Dependency aligned with oncogenic drivers: the *BRAF*
395 V600E-mutant BHT101 line was most sensitive (Chronos –1.15), followed by other *BRAF* V600E-
396 mutant lines (BCPAP, 8305C, 8505C), all showing high PDPK1 expression and strong
397 dependency (Table S4). PDPK1 expression correlated tightly with Chronos dependency ($r = 0.97$,
398 $p < 0.03$), reinforcing its functional relevance in thyroid cancer.

399 PDPK1 activity is regulated predominantly at the post-translational level; therefore,
400 messenger RNA (mRNA) or total protein abundance may not reliably reflect its functional status
401 (46). The critical activation step for PDPK1 is autophosphorylation at Ser241, which generates the
402 catalytically competent form required for downstream phosphorylation of AKT (Thr308), SGK,
403 and other AGC kinases. Because only the phosphorylated, active pool (p-PDPK1 S^{241}) propagates
404 PI3K/AKT signaling, quantifying this phosphorylated site provides a direct measure of pathway
405 engagement and oncogenic dependency. Therefore, we first characterized total and phospho-
406 PDPK1 in a panel of thyroid cancer cell lines. PDPK1 expression and phosphorylation varied in
407 the cell lines with known mutations in genes involved in the MAPK and PI3K/AKT pathways.
408 Cell lines harboring *PTEN* loss (FTC236, FTC133, and C643) and *BRAF* V600E mutations
409 (SW1736, 8505C, and BCPAP), as well as wild-type *BRAF* cell lines (THJ29T and C643) and a
410 *PIK3CA*-mutant/*MKRN1–BRAF* fusion cell line (THJ16T), all exhibited measurable PDPK1
411 expression (Fig. 1A). The phospho-PDPK1/PDPK1 ratio was markedly elevated in the FTC236,
412 C643, THJ16T, BCPAP, and 8505C cell lines relative to the HEK293 cell line (control), with the

413 THJ16T cell line demonstrating the highest PDPK1 phosphorylation, followed by the homozygous
414 *BRAF* V600E–mutant 8505C and BCPAP cell lines (Fig. 1A).

415 Consistent with MAPK pathway activation, all thyroid cancer cell lines evaluated showed
416 high MEK phosphorylation, with the *BRAF* V600E–mutant cell lines (BCPAP, 8505C, and
417 SW1736) exhibiting the highest phospho-MEK levels (Fig. 1A). The phospho-MEK/MEK ratio
418 was lower in the two patient-derived *BRAF* V600E–mutant ATC cell lines (ATC01 and ATC02)
419 compared to normal thyroid tissue, but total MEK levels were much higher in the patient-derived
420 ATC cell lines (Fig. 1B). The phospho-PDPK1/PDPK1 ratio was higher in the ATC02 cell line,
421 which was derived from a residual tumor resected after an exceptional response to combined Dab
422 and trametinib treatment, compared to the ATC01 cell line (derived tumor from a treatment-naïve
423 patient) or normal thyroid tissue. We used the *BRAF* V600E–mutant ATC cell lines (8505C and
424 SW1736) with relatively high and low phospho-PDPK1 levels and the patient-derived cell lines
425 (ATC01 and ATC02) to test the therapeutic efficacy of targeting PDPK1.

426

427 **Combined PDPK1 and BRAF V600E inhibition has synergistic anticancer activity *in vitro***
428 **and *ex vivo***

429 We evaluated drug response data from our previous drug screening studies for PDPK1
430 inhibitors in three ATC cell lines (8505C, THJ-11T, and THJ-16T), where BX795 emerged as the
431 most consistent and broadly active compound based on a half-maximal activity concentration
432 (AC_{50}) < 10 μM and **a** curve class up to –2.2. BX795 was the only agent to meet the criteria in all
433 three ATC cell lines, whereas BX-912, OSU-03012, and GSK-2334470 met the criteria in two
434 ATC cell lines, and DTXSID90678515 met the criteria in one ATC cell line (Fig. S1D). Therefore,
435 we used BX795 to inhibit PDPK1 phosphorylation. In addition, Integrated DepMap PRISM
436 analyses indicated that thyroid cancer cells are sensitive to BX795 treatment (Fig. S1E), further

437 supporting that the PDPK1 gene is essential. BX795 treatment significantly inhibited cell
438 proliferation in *BRAF* V600E–mutant ATC cell lines in a dose-dependent manner (Fig. 1C).
439 BX795 treatment reduced phosphorylation of PDPK1 at Ser241 and PI3KAKT/mTOR signaling,
440 with reduced S6K levels and upregulation of H_2AX phosphorylation (Fig. S1F). To further validate
441 the essentiality of PDPK1 and specificity of BX795 treatment, we knocked down PDPK1
442 expression. PDPK1 knockdown reduced total and phospho-PDPK1, changes associated with
443 inhibition of cellular proliferation (Fig. S1G). When combined with BX795 treatment to inhibit
444 PDPK1 phosphorylation at Ser241, there was further inhibition of cell proliferation compared to
445 the control (Fig. S1G). Collectively, the DepMap datasets and *in vitro* results suggest that targeting
446 PDPK1 for ATC therapy is a promising approach, especially in *BRAF* V600E–mutant ATC, where
447 resistance to combined BRAF and MEK inhibition is common.

448 PDPK1 inhibition with BX795 and BRAF V600E inhibition with Dab alone inhibited ATC
449 cellular proliferation (Fig. 1C–F). Combination BX795 and Dab treatment showed a synergistic
450 antiproliferative effect in *BRAF* V600E–mutant ATC cell lines at multiple dose combinations (Fig.
451 1G–J) based on a CI < 1. We selected combination concentrations (2.5 μM BX795 and 2.5 μM
452 Dab) that were synergistic and clinically achievable for the follow-up studies. Combination BX795
453 and Dab treatment significantly inhibited the size and number of ATC colonies and cellular
454 migration (Figs. 1K–N and S1H–I) compared to either agent alone or the vehicle control. BX795
455 alone and combination BX795 and Dab treatment in patient-derived *BRAF* V600E–mutant ATC
456 cells also significantly inhibited cellular proliferation (Fig. 1O–R).

457 We next tested the anticancer activity of combination BX795 and Dab treatment in *ex vivo*
458 (3D culture) model of *BRAF* V600E–mutant ATC cell lines (8505C and SW1736) and two patient-
459 derived *BRAF* V600E–mutant ATC cells (ATC01 and ATC02) that better recapitulate the
460 molecular features of human ATC and response to treatment. Dab treatment alone reduced the

461 spheroid size by ~72% (8505C) and ~56% (SW1736), and BX795 treatment alone reduced the
462 spheroid size by ~78% (8505C) and ~40% (SW1736) compared to the vehicle control;
463 combination treatment reduced the spheroid size significantly more than either agent alone (Fig.
464 1S–T). Similarly, in patient-derived ATC01 and ATC02 spheroids, combination treatment reduced
465 the spheroid size significantly more than either agent alone or the vehicle control (Fig. 1S–T).
466

467 **Combined PDPK1 and BRAF V600E inhibition has anticancer activity and is safe in *in vivo***
468 **orthotopic model of ATC**

469 We next tested combination BX795 and Dab treatment in an orthotopic mouse model using
470 the ATC *BRAF* V600E–mutant 8505C ATC cell line. BX795 and Dab treatment alone reduced the
471 tumor volume by 18% and 39%, respectively, compared to the vehicle control, whereas
472 combination BX795 and Dab treatment reduced the tumor volume by 55% compared to the vehicle
473 control (Figs. 2A and S2A–B). Combination BX795 and Dab treatment also significantly reduced
474 the tumor weight compared to the vehicle control in both genders (Fig. 2B; S2C-D). The total body
475 tumor luminescence measurement was significantly lower after treatment for 2 weeks, and the
476 growth rate was lower for the combination BX795 and Dab treatment group compared to the
477 vehicle control. Moreover, there were no metastases in any of the treatment groups (Fig. 2C–D).
478 There was no statistically significant difference in mouse weight among treatment groups, and
479 there were no treatment-related toxicities (Fig. 2E).
480

481 **Combined PDPK1 and BRAF V600E inhibition induces apoptosis**

482 To investigate the mechanism of the synergistic anticancer activity of combined PDPK1
483 and BRAF V600E inhibition, we performed TMT-based, label-intensity proteomic analysis with
484 BX795, Dab, or combination treatment. The results showed distinct pathway-selective effects with

485 monotherapy and a synergistic signaling convergence with combination treatment. Volcano plot
486 analysis demonstrated that BX795 treatment preferentially suppressed proteins involved in
487 PDPK1/AKT/mTOR signaling, ribosomal biogenesis, mitochondrial regulators, and cytoskeletal
488 organization, while inducing checkpoint- and stress-associated regulators (Fig. 3A). In contrast,
489 Dab treatment predominantly repressed MAPK-dependent proliferative and mitotic programs,
490 with compensatory activation of nuclear structural and transcriptional related proteins (Fig. 3B).
491 Combination treatment produced the greatest magnitude and breadth of proteomic remodeling,
492 marked by strong suppression of epithelial–mesenchymal transition (EMT)/metastasis-associated
493 proteins, translational machinery, and chromatin regulators, together with induction of DNA
494 damage, mitotic spindle destabilization, and apoptotic execution factors, consistent with mitotic
495 catastrophe (Fig. 3C). Venn diagram analysis revealed a conserved core of 134 shared total
496 proteins and 104 shared phosphoproteins across all three treatment groups, defining a common
497 stress-adaptive signaling module, while combination treatment uniquely altered 108 total proteins
498 and 40 phosphoproteins, indicating novel vulnerabilities unmasked only under dual pathway
499 inhibition (Fig. 3D). At the signaling level, phosphoproteomic analysis confirmed that BX795
500 suppressed PI3K/AKT/mTOR-dependent phosphorylation, Dab inhibited MEK/ERK and mitotic
501 phospho-networks, and combination treatment resulted in simultaneous shutdown of both
502 pathways, eliminating compensatory feedback upregulation. GSEA further demonstrated that
503 BX795 negatively enriched the PI3K/AKT/mTOR, mitotic spindle, oxidative phosphorylation,
504 WNT/β-catenin, and DNA repair pathways, while activating G2/M checkpoint inflammatory stress
505 and MAPK signaling. Dab suppressed MAPK-driven mitotic and metabolic programs with
506 activation of DNA repair, G2M checkpoints, EMT, p53, and oxidative phosphorylation checkpoint
507 pathways (Fig. 3E–F). Strikingly, combination treatment produced the most profound pathway-
508 level effects, with coordinated suppression of PI3K/AKT/mTOR, MAPK, WNT, mitosis,

509 oxidative phosphorylation, and DNA repair, alongside enrichment of p53, G2/M checkpoint, and
510 inflammatory response pathways, and repression of EMT signaling (Fig. 3G). Collectively, these
511 data establish that dual PDPK1 and BRAF V600E inhibition drives a synergistic, multi-layered
512 inhibition of survival, translational, cytoskeletal, mitotic, metabolic, and DNA repair networks,
513 leading to cell death.

514 To validate the proteomic results, we analyzed the canonical signaling pathways targeted
515 by BX795 and Dab, and cell death pathways. As expected, Dab reduced MEK phosphorylation,
516 and BX795 reduced PDPK1 phosphorylation at Ser^{241} (Fig. 3H). There was compensatory increase
517 in AKT^{308} + $PDPK1^{241}$ phosphorylation and MEK phosphorylation with BRAF V600E inhibition
518 alone and PDPK1 inhibition alone, respectively, but not with combined PDPK1 and BRAF V600E
519 inhibition, confirming dual pathway blockade (Fig. 3H).

520 In addition, combination PDPK1 and BRAF V600E inhibition significantly increased
521 apoptosis compared to either agent along and the vehicle control, with increased cleaved CASP3,
522 PARP-1 cleavage, decreased BCL-2, and enhanced AnnexinV/PI staining (Figs. 3H–I and S3A).
523 Furthermore, combination treatment reduced BAD phosphorylation and increased the active
524 BAD/inactive pBAD ratio by 3.4-fold and 2.4-fold in the 8505C and 2 SW1736 ATC cell lines,
525 respectively (Fig. 3J). Immunoprecipitation analysis revealing increased BCL-xL–BAD binding,
526 indicating BAD-mediated inhibition of BCL-xL's antiapoptotic function (Fig. 3K) with no binding
527 to BCL2. Furthermore, BX795 treatment reduced Ser^{9} phosphorylation (inactive) and increased
528 active GSK-3β levels, which were further enhanced with combination treatment (Fig. 3J). In
529 addition, combination PDPK1 and BRAF V600E inhibition increased γ-H2AX (Ser^{139}), indicating
530 greater DNA damage than with either agent alone and the vehicle control (Fig. 3J). Overall,
531 supervised cluster analysis demonstrated treatment-specific differential abundance across extrinsic
532 death receptor components (TNFRSF10A and FAS), mitochondrial apoptosis regulators (BAD,

533 BID, BAX, BAK1, and BCL2L1), and executioners of apoptosis (CASP3, CASP7, CASP8, and
534 CASP9), with a distinct expression signature including BAD, BAX, BCL2, CASP3, and PARP1
535 observed with combination treatment (Fig. 3L). Combination treatment led to higher levels of BID,
536 CASP3, and BAD and lower levels of BCL2L1 and PARP1. Although the total BAX and BCL2
537 protein levels were lower, the BAX/BCL2 ratio was high after combination treatment compared
538 to either agent alone, further supporting enhanced apoptosis (Fig. 3L), Together, these results show
539 that combination treatment synergistically induces apoptosis, activates caspase, leads to DNA
540 damage, and suppresses survival signaling pathways in *BRAF* V600E–mutant ATC cells.
541

542 **Combination BX795 and Dab treatment induces DNA damage and G2 cell cycle arrest in**
543 **ATC cells**

544 To assess DNA damage induced by combination treatment, we evaluated the formation of
545 γH2AX (Ser139) foci. Both BX795 and Dab treatment alone increased γH2AX, with combination
546 treatment resulting in the highest number of foci, γH2AX-positive cells, and fluorescence intensity
547 (Fig. 3M). Furthermore, DNA damage response activation was highest with combination
548 treatment, with a greater increase in ATM (Ser^{1981}) and CHK2 (T^{68}) phosphorylation, while CHK1
549 (Ser^{345}) phosphorylation increased with Dab treatment, decreased with BX795 treatment, and had
550 an intermediate effect with combination treatment (Fig. 3N).

551 Cell cycle analysis showed BX795 induced strong G2/M arrest, Dab caused G0/G1 arrest,
552 and combination treatment significantly increased G2/M arrest with 4N DNA accumulation (Fig.
553 3O). BX795 increased cyclin B, which was further elevated with combination treatment, while
554 both agents alone reduced the CDK1/pCDK1 ratio, PLK1 phosphorylation, and phospho-CDC25C
555 (Thr^{48}), with the strongest effect observed with combination treatment (Fig. 3P). Combination
556 treatment also lowered cyclin A2 and depleted phospho-histone H3 (Ser^{10}), and disrupted spindle

557 microtubule assembly in nocodazole-synchronized cells, indicating failure to progress from the
558 G2 phase to the M phase despite cyclin B accumulation. Likewise, Dab treatment reduced cyclin
559 D1, which was further reduced with combination treatment due to proteasomal degradation;
560 however, BX795 treatment alone had no effect (Fig. 3Q). Together, these data demonstrate that
561 combined PDPK1 and BRAF inhibition synergistically disrupts cell-cycle progression by
562 enforcing G2/M arrest with defective mitotic entry, accompanied by proteasomal degradation of
563 cyclin D1.

564 We further assessed DNA damage responses associated with combination treatment–
565 induced G2 arrest based on the phosphoproteomic results. Combination treatment resulted in the
566 highest phosphorylation of RAD50, CDK1, MCM2, PRKDC, and XRCC5 compared with either
567 agent alone (Fig. 3R), consistent with enhanced sensing of double-stranded DNA (dsDNA) breaks,
568 replication stress, reinforced G2/M checkpoint activation, and increased engagement of non-
569 homologous end joining (NHEJ)-mediated repair. In contrast, combination treatment reduced the
570 abundance of LIG1, MDC1, and MSH6 relative to treatment with either agent alone, indicating
571 suppression of DNA repair synthesis, chromatin-based damage signaling, and mismatch repair
572 pathways (Fig. 3R). Together, these findings indicate that combination treatment leads to a greater
573 DNA damage burden marked by replication stress, checkpoint activation, and NHEJ engagement,
574 while suppressing key DNA repair scaffolding and mismatch repair components.

575 Taken together, these findings suggest that dual PDPK1 and BRAF V600E inhibition
576 activates ATM/CHK2 signaling, downregulates G2/M regulators, blocks mitotic entry, and
577 enforces persistent G2 arrest in ATC cells.

578

579 **Combination BX795 and Dab treatment induces mitotic G2 arrest that is associated with**
580 **mitochondrial dysfunction**

581 Given that prolonged cell cycle arrest can result in oxidative stress, we assessed ROS levels
582 following treatment with BX795, Dab, or their combination in *BRAF* V600E–mutant ATC cells.
583 Combination treatment markedly increased intracellular ROS (DCFH-DA) and mitochondrial
584 superoxide (MitoSOX) compared with either agent alone or the vehicle control (Fig. 4A–B).
585 MitoTracker Green staining revealed increased mitochondrial content that was most pronounced
586 with combination treatment (Fig. 4C–D), accompanied by a higher mitochondrial membrane
587 potential (TMRM) without loss of integrity (Fig. 4E).

588 Seahorse analysis showed that combination treatment significantly reduced basal, ATP-
589 linked, and maximal respiration, indicating impairment in oxidative phosphorylation (Figs. 4F and
590 S4A). Mitochondrial integrity was also confirmed by JC-1 staining (Fig. S4B). Profiling of
591 proteins related to oxidative phosphorylation revealed complex, specific changes with combined
592 treatments, where complex V increased in both *BRAF* V600E–mutant ATC cell lines. On the other
593 hand, relative to the vehicle control, complex III was higher in 8505C cells, while complex II and
594 IV were higher in SW1736 cells (Fig. S4C).

595 We performed supervised cluster analysis of the proteomic data to determine the effect of
596 BX795, Dab, and their combination on proteins involved in mitochondrial ribosomal function,
597 electron transport chain complexes, the tricarboxylic acid (TCA) cycle, mitochondrial dynamics,
598 and metabolite transport (Fig. 5G). We found higher relative abundance of mitochondrial
599 respiratory chain and metabolic enzymes with BX795 treatment, including multiple complex I
600 subunits (NDUFS1, NDUFS7, NDUFS2, NDUFS3, NDUFV1, and NDUFB8), complex II
601 components (SDHA, SDHB, SDHC, and SDHD), complex III proteins (UQCRC1 and UQCRC2),
602 complex IV subunits (COX5A, COX4I1, COX6C, COX7C, COX5B, and COX7A2), and ATP
603 synthase subunits (ATP5F1A, ATP5F1B, ATP5F1C, ATP5PB, and ATP5PF). There was reduced
604 relative abundance with Dab treatment and markedly reduced abundance with combination

605 treatment. Proteins involved in the TCA cycle and mitochondrial metabolism, including IDH1,
606 IDH2, IDH3A, IDH3B, FH, OGDH, DLST, MDH2, CS, PDHA1, PDHB, PC, DLD, GLUD1,
607 ACADM, and ACADVL, followed a similar pattern, with higher expression with BX795
608 treatment, intermediate or reduced expression with Dab treatment, and the lowest relative
609 abundance with combination treatment.

610 Mitochondrial structure, dynamics, and transport proteins, including TFAM, TOMM20,
611 TIMM23, MFN1, OPA1, DNM1L, VDAC1, VDAC2, and VDAC3, also a demonstrated
612 progressive reduction from BX795 to Dab treatment, and a further reduction with combination
613 treatment. CYCS and HSPA9 displayed higher abundance with BX795 treatment, reduced
614 abundance with Dab treatment, and further reduction with combination treatment. Collectively,
615 these data demonstrate broad and coordinated suppression of mitochondrial oxidative
616 phosphorylation, TCA cycle activity, and mitochondrial structural components with combination
617 treatment, with intermediate effects observed with Dab treatment alone and the highest relative
618 expression with BX795 treatment.

619 The consistent decrease in mitochondrial complex proteins supports that mitochondrial
620 dysfunction occurs with dual PDPK1 and BRAF V600E inhibition. This triggers ROS generation
621 even though the mitochondrial membrane potential is preserved. These changes are consistent with
622 a glycolytic, senescence-like phenotype as described previously (47).

623

624 **ROS scavenging mitigates genotoxicity while CHK2 inhibition induces mitotic slippage and**
625 **partially reverses combination therapy-induced apoptosis**

626 Next, we preformed time-course analysis to determine the sequence of events with
627 combination treatment that leads to its synergistic anticancer activity. We found G2/M arrest
628 occurred by 6 h; this preceded ROS elevation (which began at 12 h) (Fig. 5A–B). The

629 mitochondrial membrane potential increased as early as 6 h, while mitochondrial accumulation
630 occurred later (≥ 20 h) (Fig. S4D–E). Thus, combination treatment induces early G2/M arrest and
631 mitochondrial hyperpolarization, followed by sustained ROS production in *BRAF* V600E–mutant
632 ATC cells. To assess the role of ROS in combination treatment–induced cytotoxicity, we used the
633 ROS scavengers *N*-acetyl cysteine (NAC) and MitoQ. NAC significantly reduced combination
634 treatment–induced ROS (DCFH-DA) (Fig. 5C), apoptosis (Annexin V/PI) (Fig. 5D), and PARP
635 cleavage (Fig. 5E), indicating ROS-mediated apoptosis. NAC treatment also decreased γ-H_2AX
636 and DNA damage response proteins (pATM and pCHK2) but did not reverse G2 arrest (Fig. S4F),
637 suggesting ROS generation occurs downstream of cell cycle arrest. MitoQ treatment partially
638 released cells from G2 arrest (Fig. 5F), implicating mitochondrial superoxide in cell cycle
639 regulation.

640 Next, to explore the involvement of CHKs in combination treatment–induced cell cycle
641 arrest, we used the CHK2 inhibitor BML-277, which significantly reversed combination
642 treatment–induced G2 arrest (Figs. 5G and S4G), cell proliferation (Fig. 5H), and apoptosis (Fig.
643 5I) in 8505C cells. As CHK1 and CHK2 both were active in SW1736 cells, we used AZD7762
644 (which inhibits both CHK1 and CHK2) in SW1736 cells, which resulted in mitotic slippage (Fig.
645 S4H) and reversed the inhibition of cellular proliferation (Fig. S4I). These data suggest that mitotic
646 arrest leads to apoptosis, which can be partially reversed by mitotic slippage.

647

648 **DISCUSSION**

649 PDPK1 is overexpressed in thyroid cancer (39). High PDPK1 levels in thyroid cancer are
650 associated with advanced stage, larger tumor size, lymph node metastasis, ATC, and worse overall
651 and recurrence-free survival (48). In this study, we found high levels of total and phosphorylated
652 PDPK1 at Ser241 in ATC cells, and combined inhibition of PDPK1 and BRAF V600E had

653 synergistic anticancer activity in *BRAF* V600E–mutant ATC in *in vitro*, *ex vivo*, and *in vivo*
654 models. Mechanistically, this combination effectively suppressed both the PDPK1/AKT and
655 MAPK pathways without rebound activation that is seen with inhibition of a single pathway. Dual
656 inhibition resulted in pronounced DNA damage, G2 cell cycle arrest, and apoptosis in *BRAF*
657 V600E–mutant ATC cells.

658 Dual inhibition of PDPK1 and mutant *BRAF* V600E–mutant ATC drives accumulation of
659 dsDNA damage and G2 arrest through complementary mechanisms, where *BRAF* V600E
660 inhibition induces replication stress by abruptly halting MAPK-driven proliferation, generating
661 stalled replication forks that can collapse into dsDNA breaks (49). PDPK1 blockade suppresses
662 AKT and other AGC kinase signaling, impairing key DNA repair pathways including homologous
663 recombination and NHEJ, thereby preventing resolution of these molecular events (50,51). The
664 resulting accumulation of unrepaired DNA damage activates the G2/M checkpoint, enforcing cell
665 cycle arrest and sensitizing cells to apoptosis (52). We found the combined inhibition of PDPK1
666 and *BRAF* V600E results in accumulation of unrepaired DNA damage, which activates the G2/M
667 checkpoint and enhances apoptotic commitment, as observed in our cell viability and apoptosis
668 assays. Interestingly, this genotoxic stress is also accompanied by mitochondrial dysfunction,
669 characterized by disrupted oxidative phosphorylation and an unexpected increase in the
670 mitochondrial membrane potential, without triggering mitochondrial outer membrane
671 permeabilization. This hyperpolarized mitochondrial state likely reflects an adaptive response to
672 maintain ATP production under DNA damage–induced metabolic stress, consistent with previous
673 observations that DNA damage can alter mitochondrial bioenergetics and promote mitochondrial
674 hyperpolarization (53,54). This mechanistic interplay aligns with studies linking cell cycle
675 checkpoint disruption to mitochondrial dysfunction, ROS accumulation, and apoptotic priming
676 (55).

677 Treatment with the mitochondria-targeted antioxidant MitoQ partially reduced G2 arrest,
678 suggesting that mitochondrial ROS and hyperpolarization contribute to the enforcement of cell
679 cycle checkpoints. This is consistent with reports that mitochondrial ROS can act as signaling
680 intermediates to activate DNA damage checkpoints and maintain G2 arrest (53,56). These findings
681 imply that mitochondrial bioenergetic stress is not merely a byproduct of DNA damage but
682 actively reinforces G2/M checkpoint signaling. Therapeutically, this highlights that combined
683 inhibition of PDPK1 and BRAF V600E exploits a dual vulnerability: suppression of proliferative
684 signaling and engagement of DNA damage responses. These results highlight a feed-forward
685 mechanism where mitochondrial dysfunction amplifies cell cycle arrest, providing a therapeutic
686 vulnerability that is exploitable by combined inhibition of PDPK1 and BRAF V600E.

687 Dual inhibition of PDPK1 and *BRAF* V600E promoted dsDNA breaks and oxidative stress.
688 Notably, treatment with the ROS scavenger NAC attenuated apoptosis and reduced DNA damage
689 but did not reverse G2 arrest, indicating that mitochondrial ROS primarily function downstream
690 of cell cycle checkpoint activation to drive cell death rather than initiating the arrest itself. NAC
691 primarily scavenges H_2O_2, HOCl, and •OH, increasing GSH levels (57), whereas MitoQ targets
692 mitochondrial superoxide and H_2O_2 (58). Because ROS species can propagate via chain reactions
693 (59,60), MitoQ-mediated arrest release supports a role for mitochondrial superoxide in sustaining
694 G2 arrest during combination treatment. These findings suggest a model in which DNA damage
695 response–mediated G2 arrest primes mitochondria toward a hyperpolarized, pro-apoptotic state,
696 with oxidative stress acting as a critical amplifier of apoptosis in ATC cells (53,56). Although the
697 OCR was not reduced, mitochondrial hyperpolarization reflects impaired proton dissipation and
698 electron congestion within the electron transport chain rather than enhanced oxidative
699 phosphorylation, a characteristic feature of dysfunctional, ROS-producing mitochondria (61).
700 BAD phosphorylation by AKT and RSK1—regulated by PDPK1 and MAPK—leads to

701 inactivation and sequestration by 14-3-3 proteins, a mechanism linked to BRAF inhibitor
702 resistance in melanoma (62). Inhibiting PI3K/PDPK1/AKT and BRAF pathways prevents BAD
703 sequestration and promotes active BAD driven apoptosis (63–65). This mechanism underscores
704 the therapeutic potential of combining PDPK1 and BRAF V600E inhibition to simultaneously
705 enforce cell cycle blockade and trigger ROS-dependent apoptotic pathways.

706 ATC harbors frequent mutations in genes that lead to activation of both the
707 PI3K/AKT/mTOR and MAPK signaling pathways. Activating mutations in PIK3CA occur in
708 approximately 10%–20% of ATC cases, while PTEN loss or inactivating mutations are also
709 common, collectively promoting constitutive PI3K/AKT signaling (4,66,67). In parallel, MAPK
710 pathway activation is highly prevalent, with *BRAF* V600E mutations detected in 40%–70% of
711 ATC cases, and RAS mutations contributing to MAPK hyperactivation in a significant subset
712 (4,68). These two pathways are activated in ATC, reinforcing proliferative, survival, and stress-
713 adaptive signaling. Their combined deregulation underpins therapeutic resistance to *BRAF* V600E
714 inhibitors and a poor prognosis in ATC (63,69,70), underscoring the need for rational dual-
715 targeting strategies. PDPK1 represents a strategic therapeutic node in ATC because it lies
716 downstream of PI3K and integrates signals from multiple recurrent alterations, including *PIK3CA*,
717 *PTEN*, and *RAS*. Selective inhibition of PI3K or AKT may leave bypass pathways intact. On the
718 other hand, PDPK1 activates a broad network of AGC kinases (AKT, SGK, S6K, and PKC
719 isoforms), making it a more effective point of signaling blockade. By targeting PDPK1, both
720 survival signaling and stress-adaptation programs are disrupted, addressing the multifaceted
721 oncogenic landscape of ATC.

722 The therapeutic implications of our findings are immediate. Dab is a Food and Drug
723 Administration–approved inhibitor of BRAF V600E, while the PDPK1 inhibitor BX795 has
724 antitumor activity in *in vitro*, *ex vivo*, and *in vivo* models of ATC and resulted in no treatment-

725 related toxicity alone or in combination with Dab *in vivo*. Our data show that PDPK1 inhibition
726 exerts intrinsic anticancer activity and significantly enhances BRAF V600E inhibition, supporting
727 a rational, dual-targeted approach. Given that both compounds have been validated preclinically
728 and/or clinically, this combination represents an opportunity to translate this combination into an
729 early-phase clinical trial in *BRAF* V600E–mutant ATC. Moreover, because *BRAF* V600E is
730 present in ~15% of all human cancers, this strategy may extend beyond ATC to other malignancies
731 driven by MAPK and PI3K/AKT/mTOR crosstalk.

732 In summary, we have identified PDPK1 as a critical therapeutic vulnerability in ATC. By
733 functioning as a central effector of PI3K/AKT/mTOR signaling, PDPK1 integrates multiple
734 oncogenic inputs common in ATC, and its inhibition disrupts both survival and stress-adaptation
735 pathways. Importantly, combining PDPK1 inhibition with BRAF blockade yields synergistic
736 anticancer activity. These findings provide a strong rationale for advancing PDPK1 inhibition,
737 particularly in combination with *BRAF* V600E inhibition, into the clinic.

738

739 **Funding declaration**

740 Early drug screening work was supported through the National Cancer Institute, National
741 Institutes of Health (ZIABC011286-09). The remainder of the research was supported through the
742 Stanford Medicine Harry A. Oberhelman Jr. and Mark L. Welton endowment at Stanford
743 University.

744

745 **Author Contribution declaration**

746 Tejinder Pal Khaket: Conceptualization, Methodology, Validation, Investigation, Visualization,
747 Writing- Original draft preparation. Chandrayee Ghosh, Zhongyue Yang, Jiangnan Hu, Eden D.
748 Alamaw, Myriem Boufraqech, Thorkell Andresson Maura O'Neill, Ya-Qin Zhang, Min Shen,

Bereketeab Haileselassie: Visualization, Investigation, Data curation, Methodology. Electron Kebebew: Supervision, Conceptualization, Project administration, Writing- Reviewing and Editing, Funding acquisition.

Declaration of Competing Interest

The authors declare that they have no known competing financial interests or personal relationships that could have appeared to influence the work reported in this paper.

Consent to Publish declaration: Not applicable

Ethics Approval and Consent to Participate

Patient-derived tumor samples were obtained under protocols approved by the Stanford University Institutional Review Board (IRB protocol 50782). All samples were collected with written informed consent from participants in accordance with institutional guidelines. No identifying information was used.

All animal procedures were approved by the Stanford Administrative Panel on Laboratory Animal Care (APLAC; Protocol #34767) and conducted in accordance with institutional and federal guidelines.

Availability of data and materials: All data generated or analyzed during this study are presented within the manuscript and its supplementary materials. Any additional information or raw datasets can be obtained from the corresponding author upon reasonable request.

References

773 1. Kebebew E, Greenspan FS, Clark OH, Woeber KA, McMillan A. Anaplastic thyroid
774 carcinoma. Treatment outcome and prognostic factors. Cancer 2005;103:1330–5.
775 2. Nilubol N, Kebebew E. Should small papillary thyroid cancer be observed? A
776 population-based study. Cancer 2015;121:1017–24.
777 3. Bible KC, Kebebew E, Brierley J et al. 2021 American Thyroid Association Guidelines
778 for management of patients with anaplastic thyroid cancer. Thyroid 2021;31:337–86.
779 4. Landa I, Ibrahimpasic T, Boucai L et al. Genomic and transcriptomic hallmarks of poorly
780 differentiated and anaplastic thyroid cancers. J Clin Invest 2016;126:1052–66.
781 5. Tiedje V, Ting S, Herold T et al. NGS based identification of mutational hotspots for
782 targeted therapy in anaplastic thyroid carcinoma. Oncotarget 2017;8:42613–20.
783 6. Feldman RI, Wu JM, Polokoff MA et al. Novel small molecule inhibitors of 3-
784 phosphoinositide-dependent kinase-1. J Biol Chem 2005;280:19867–74.
785 7. Subbiah V, Kreitman RJ, Wainberg ZA et al. Dabrafenib and trametinib treatment in
786 Patients with locally advanced or metastatic BRAF V600-mutant anaplastic thyroid
787 cancer. J Clin Oncol 2018;36:7–13.
788 8. Wang VE, Xue JY, Frederick DT et al. Adaptive resistance to dual BRAF/MEK
789 inhibition in BRAF-driven tumors through autocrine FGFR pathway activation. Clin
790 Cancer Res 2019;25:7202–17.
791 9. Montero-Conde C, Ruiz-Llorente S, Dominguez JM et al. Relief of feedback inhibition of
792 HER3 transcription by RAF and MEK inhibitors attenuates their antitumor effects in
793 BRAF-mutant thyroid carcinomas. Cancer Discov 2013;3:520–33.
794 10. Xu B, Fuchs T, Dogan S et al. Dissecting anaplastic thyroid carcinoma: A comprehensive
795 clinical, histologic, immunophenotypic, and molecular study of 360 cases. Thyroid
796 2020;30:1505–17.

797 11. Kandil E, Tsumagari K, Ma J et al. Synergistic inhibition of thyroid cancer by
798 suppressing MAPK/PI3K/AKT pathways. J Surg Res 2013;184:898–906.
799 12. Castellano E, Downward J. RAS interaction with PI3K: More than just another effector
800 pathway. Genes Cancer 2011;2:261–74.
801 13. Chi M, Ye Y, Zhang XD, Chen J. Insulin induces drug resistance in melanoma through
802 activation of the PI3K/Akt pathway. Drug Des Devel Ther 2014;8:255–62.
803 14. Jiang CC, Lai F, Thorne RF et al. MEK-independent survival of B-RAFV600E
804 melanoma cells selected for resistance to apoptosis induced by the RAF inhibitor
805 PLX4720. Clin Cancer Res 2011;17:721–30.
806 15. Byeon HK, Na HJ, Yang YJ et al. Acquired resistance to BRAF inhibition induces
807 epithelial-to-mesenchymal transition in BRAF (V600E) mutant thyroid cancer by c-Met-
808 mediated AKT activation. Oncotarget 2017;8:596–609.
809 16. Byeon HK, Na HJ, Yang YJ et al. c-Met-mediated reactivation of PI3K/AKT signaling
810 contributes to insensitivity of BRAF(V600E) mutant thyroid cancer to BRAF inhibition.
811 Mol Carcinog 2016;55:1678–87.
812 17. Guo H, German P, Bai S et al. The PI3K/AKT pathway and renal cell carcinoma. J Genet
813 Genomics 2015;42:343–53.
814 18. Gagliardi PA, Puliafito A, Primo L. PDK1: At the crossroad of cancer signaling
815 pathways. Semin Cancer Biol 2018;48:27–35.
816 19. Dangelmaier C, Manne BK, Liverani E, Jin J, Bray P, Kunapuli SP. PDK1 selectively
817 phosphorylates Thr(308) on Akt and contributes to human platelet functional responses.
818 Thromb Haemost 2014;111:508–17.

819 20. Zabkiewicz J, Pearn L, Hills RK et al. The PDK1 master kinase is over-expressed in
820 acute myeloid leukemia and promotes PKC-mediated survival of leukemic blasts.
821 Haematologica 2014;99:858–64.
822 21. Pearn L, Fisher J, Burnett AK, Darley RL. The role of PKC and PDK1 in monocyte
823 lineage specification by Ras. Blood 2007;109:4461–9.
824 22. Maurer M, Su T, Saal LH et al. 3-Phosphoinositide-dependent kinase 1 potentiates
825 upstream lesions on the phosphatidylinositol 3-kinase pathway in breast carcinoma.
826 Cancer Res 2009;69:6299–306.
827 23. Du J, Yang M, Chen S, Li D, Chang Z, Dong Z. PDK1 promotes tumor growth and
828 metastasis in a spontaneous breast cancer model. Oncogene 2016;35:3314–23.
829 24. Lohneis P, Darb-Esfahani S, Dietel M, Braicu I, Sehouli J, Arsenic R. PDK1 is expressed
830 in ovarian serous carcinoma and correlates with improved survival in high-grade tumors.
831 Anticancer Res 2015;35:6329–34.
832 25. Ahmed N, Riley C, Quinn MA. An immunohistochemical perspective of PPAR beta and
833 one of its putative targets PDK1 in normal ovaries, benign and malignant ovarian
834 tumours. Br J Cancer 2008;98:1415–24.
835 26. Choucair KA, Guerard KP, Ejdelman J et al. The 16p13.3 (PDPK1) genomic gain in
836 prostate cancer: A potential role in disease progression. Transl Oncol 2012;5:453–60.
837 27. Jiang Q, Zheng N, Bu L et al. Correction: SPOP-mediated ubiquitination and degradation
838 of PDK1 suppresses AKT kinase activity and oncogenic functions. Mol Cancer
839 2025;24:137.
840 28. Scortegagna M, Ruller C, Feng Y et al. Genetic inactivation or pharmacological
841 inhibition of Pdk1 delays development and inhibits metastasis of Braf(V600E)::Pten(-/-)
842 melanoma. Oncogene 2014;33:4330–9.

843 29. Emmanouilidi A, Fyffe CA, Ferro R et al. Preclinical validation of 3-phosphoinositide-
844 dependent protein kinase 1 inhibition in pancreatic cancer. J Exp Clin Cancer Res
845 2019;38:191.
846 30. Casari I, Domenichini A, Sestito S et al. Dual PDK1/aurora kinase A inhibitors reduce
847 pancreatic cancer cell proliferation and colony formation. Cancers (Basel) 2019;11.
848 31. Wu N, He C, Zhu B, Jiang J, Chen Y, Ma T. 3-Phosphoinositide dependent protein
849 kinase-1 (PDK-1) promotes migration and invasion in gastric cancer cells through
850 activating the NF-kappaB pathway. Oncol Res 2017;25:1153–59.
851 32. Bai X, Li P, Xie Y et al. Overexpression of 3-phosphoinositide-dependent protein kinase-
852 1 is associated with prognosis of gastric carcinoma. Tumour Biol 2016;37:2333–9.
853 33. Wang J, Liu F, Ao P et al. Correlation of PDK1 expression with clinicopathologic
854 features and prognosis of hepatocellular carcinoma. Onco Targets Ther 2016;9:5597–
855 602.
856 34. Yang Z, Wu Z, Liu T et al. Upregulation of PDK1 associates with poor prognosis in
857 esophageal squamous cell carcinoma with facilitating tumorigenicity in vitro. Med Oncol
858 2014;31:337.
859 35. Luo D, Xu X, Li J et al. The PDK1/c-Jun pathway activated by TGF-beta induces EMT
860 and promotes proliferation and invasion in human glioblastoma. Int J Oncol
861 2018;53:2067–80.
862 36. Jing P, Zhou S, Xu P et al. PDK1 promotes metastasis by inducing epithelial-
863 mesenchymal transition in hypopharyngeal carcinoma via the Notch1 signaling pathway.
864 Exp Cell Res 2020;386:111746.

865 37. Tang N, Hu B, Zhang Y, Chen Z, Yu R. Possible involvement of the Hedgehog and
866 PDPK1-Akt pathways in the growth and migration of small-cell lung cancer. J Int Med
867 Res 2021;49:3000605211016562.
868 38. Zhang X, Yu Z. Expression of PDK1 in malignant pheochromocytoma as a new
869 promising potential therapeutic target. Clin Transl Oncol 2019;21:1312–8.
870 39. Sun Z, Xu L. Expression of PDK-1 and DMBT1 in the thyroid carcinoma and its
871 clinicopathological significance. Oncol Lett 2019;18:2819–24.
872 40. Lin HJ, Hsieh FC, Song H, Lin J. Elevated phosphorylation and activation of PDK-
873 1/AKT pathway in human breast cancer. Br J Cancer 2005;93:1372–81.
874 41. Bamodu OA, Chang HL, Ong JR, Lee WH, Yeh CT, Tsai JT. Elevated PDK1 expression
875 drives PI3K/AKT/MTOR signaling promotes radiation-resistant and dedifferentiated
876 phenotype of hepatocellular carcinoma. Cells 2020;9.
877 42. Choi JH, Yang YR, Lee SK et al. Potential inhibition of PDK1/Akt signaling by
878 phenothiazines suppresses cancer cell proliferation and survival. Ann N Y Acad Sci
879 2008;1138:393–403.
880 43. Nagashima K, Shumway SD, Sathyanarayanan S et al. Genetic and pharmacological
881 inhibition of PDK1 in cancer cells: characterization of a selective allosteric kinase
882 inhibitor. J Biol Chem 2011;286:6433–48.
883 44. Ding L, Ren C, Yang L et al. OSU-03012 disrupts Akt signaling and prevents
884 endometrial carcinoma progression in vitro and in vivo. Drug Des Devel Ther
885 2021;15:1797–810.
886 45. Chou TC. Drug combination studies and their synergy quantification using the Chou-
887 Talalay method. Cancer Res 2010;70:440–6.

888 46. Bayascas JR, Wullschleger S, Sakamoto K et al. Mutation of the PDK1 PH domain
889 inhibits protein kinase B/Akt, leading to small size and insulin resistance. Mol Cell Biol
890 2008;28:3258–72.
891 47. Correia-Melo C, Marques FD, Anderson R et al. Mitochondria are required for pro-
892 ageing features of the senescent phenotype. EMBO J 2016;35:724–42.
893 48. Wang M, Mao C, Ouyang L et al. Pathological and prognostic role of PDK1 in papillary
894 thyroid carcinoma. Biochem Biophys Res Commun 2020;524:338–44.
895 49. Yang C, Tian C, Hoffman TE, Jacobsen NK, Spencer SL. Melanoma subpopulations that
896 rapidly escape MAPK pathway inhibition incur DNA damage and rely on stress
897 signalling. Nat Commun 2021;12:1747.
898 50. Fraser M, Harding SM, Zhao H, Coackley C, Durocher D, Bristow RG. MRE11
899 promotes AKT phosphorylation in direct response to DNA double-strand breaks. Cell
900 Cycle 2011;10:2218–32.
901 51. Toulany M, Lee KJ, Fattah KR et al. Akt promotes post-irradiation survival of human
902 tumor cells through initiation, progression, and termination of DNA-PKcs-dependent
903 DNA double-strand break repair. Mol Cancer Res 2012;10:945–57.
904 52. Stommel JM, Kimmelman AC, Ying H et al. Coactivation of receptor tyrosine kinases
905 affects the response of tumor cells to targeted therapies. Science 2007;318:287–90.
906 53. Zorov DB, Juhaszova M, Sollott SJ. Mitochondrial reactive oxygen species (ROS) and
907 ROS-induced ROS release. Physiol Rev 2014;94:909–50.
908 54. Wang X, Lim, HJ, Son YO. Down-regulation of mitochondrial voltage-dependent anion
909 channel (VDAC) contributes to protective effect of DNA damage on apoptosis. J Biol
910 Chem 2010;285:34960–70.

911 55. Raimundo N, Song L, Shutt TE et al. Mitochondrial stress engages E2F1 apoptotic
912 signaling to cause deafness. Cell 2012;148:716–26.
913 56. Srinivas US, Tan BWQ, Vellayappan BA, Jeyasekharan AD. ROS and the DNA damage
914 response in cancer. Redox Biol 2019;25:101084.
915 57. Pedre B, Barayeu U, Ezerina D, Dick TP. The mechanism of action of N-acetylcysteine
916 (NAC): The emerging role of H(2)S and sulfane sulfur species. Pharmacol Ther
917 2021;228:107916.
918 58. Sena LA, Chandel NS. Physiological roles of mitochondrial reactive oxygen species. Mol
919 Cell 2012;48:158–67.
920 59. Khaket TP, Ahmad R. Biochemical studies on hemoglobin modified with reactive
921 oxygen species (ROS). Appl Biochem Biotechnol 2011;164:1422–30.
922 60. Collin F. Chemical basis of reactive oxygen species reactivity and involvement in
923 neurodegenerative diseases. Int J Mol Sci 2019;20.
924 61. Brand MD, Nicholls DG. Assessing mitochondrial dysfunction in cells. Biochem J
925 2011;435:297–312.
926 62. Perna D, Karreth FA, Rust AG et al. BRAF inhibitor resistance mediated by the AKT
927 pathway in an oncogenic BRAF mouse melanoma model. Proc Natl Acad Sci U S A
928 2015;112:E536–45.
929 63. Scheid MP, Duronio V. Dissociation of cytokine-induced phosphorylation of Bad and
930 activation of PKB/akt: involvement of MEK upstream of Bad phosphorylation. Proc Natl
931 Acad Sci U S A 1998;95:7439–44.
932 64. She QB, Solit DB, Ye Q, O'Reilly KE, Lobo J, Rosen N. The BAD protein integrates
933 survival signaling by EGFR/MAPK and PI3K/Akt kinase pathways in PTEN-deficient
934 tumor cells. Cancer Cell 2005;8:287–97.

935 65. Fang X, Yu S, Eder A et al. Regulation of BAD phosphorylation at serine 112 by the
936 Ras-mitogen-activated protein kinase pathway. Oncogene 1999;18:6635–40.
937 66. Ricarte-Filho JC, Ryder M, Chitale DA et al. Mutational profile of advanced primary and
938 metastatic radioactive iodine-refractory thyroid cancers reveals distinct pathogenetic roles
939 for BRAF, PIK3CA, and AKT1. Cancer Res 2009;69:4885–93.
940 67. Pozdeyev N, Gay LM, Sokol ES et al. Genetic analysis of 779 advanced differentiated
941 and anaplastic thyroid cancers. Clin Cancer Res 2018;24:3059–68.
942 68. Xing M. Molecular pathogenesis and mechanisms of thyroid cancer. Nat Rev Cancer
943 2013;13:184–99.
944 69. Gowrishankar K, Snoyman S, Pupo GM, Becker TM, Kefford RF, Rizos H. Acquired
945 resistance to BRAF inhibition can confer cross-resistance to combined BRAF/MEK
946 inhibition. J Invest Dermatol 2012;132:1850–9.
947 70. Villanueva J, Vultur A, Lee JT et al. Acquired resistance to BRAF inhibitors mediated by
948 a RAF kinase switch in melanoma can be overcome by cotargeting MEK and IGF-
949 1R/PI3K. Cancer Cell 2010;18:683–95.
950
951
952
953
954
955
956
957
958

959 **Fig. 1: Combined PDPK1 and BRAF V600E inhibition has synergistic anticancer activity *in***
960 ***vitro* and *ex vivo*.**
961 (A) Immunobloting of pPDPK1, PDPK1, pMEK, and MEK in thyroid cancer lines: papillary
962 thyroid cancer (PTC, brown color) (TPC1), follicular thyroid cancer (FTC, blue color) (FTC-133
963 and FTC-236), poorly differentiated thyroid cancer (PDTC, green color) (BCPAP), *BRAF* wild
964 type anaplastic thyroid cancer (ATC) (red color) (C643 and THJ29T), *BRAF*V600E–mutant ATC
965 (8505C, SW1736, and THJ16T), and HEK293 cells using β-actin as a loading control. The relative
966 ratio of pPDPK1 to total PDPK1 and pMEK to total MEK is listed below each phospho-protein
967 compared to HEK293 cells. (B) Immunoblotting of phosphoPDPK1, total PDPK1 in untreated and
968 dabrafenib (Dab) and trametinib–treated patient derived ATC and normal thyroid tissues using β-
969 actin as a loading control. The relative ratio of pPDPK1 to total PDPK1 and pMEK to total MEK
970 is listed below each phospho-protein compared to normal thyroid tissue. (C–D) Dose-dependent
971 inhibition of cell proliferation with BX795 treatment in 8505C and SW1736 cells after 48 h. (E–
972 F) Dose-dependent inhibition of cell proliferation with Dab treatment in 8505C and SW1736 ATC
973 cells after 48 h. (G–H) Analysis of the combination index (CI) using the CompuSyn software for
974 BX795, Dab, and their combination in *BRAF* V600E–mutant ATC cell lines. CI < 1 indicates
975 synergism, and fa denotes fraction affected. (I–J) The effect of BX795 (2.5 μM), Dab (2.5 μM),
976 and their combination on cellular proliferation in 8505C and SW1736 cells after 48 h. (K–L)
977 Colony-formation assay in 8505C and SW1736 cells treated with BX795 (2.5 μM), Dab (2.5 μM),
978 or their combination. Quantification was performed using ImageJ. (M–N) Cellular migration as
979 measured with a wound-healing assay in 8505C and SW1736 cells treated with BX795 (2.5 μM),
980 Dab (2.5 μM), or their combination. Quantification was performed using the ImageJ software. (O–
981 P) Concentration-dependent effects of BX795 treatment on proliferation of patient-derived ATC
982 cells (ATC01 and ATC02). ATC01 was derived from a treatment-naïve patient tumor positive for
983 *BRAF* V600E mutation, and ATC02 was derived from a residual tumor in a patient with an
984 exceptional treatment response to Dab and trametinib, and the tumor was positive for *BRAF* V600E
985 mutation. (Q–R) The effects of treatment with BX795 (2.5 μM), Dab (2.5 μM), or their
986 combination on the proliferation of patient-derived ATC cells (ATC01 and ATC02). (S) The effect
987 of treatment with BX795 (2.5 μM), Dab (2.5 μM), or their combination on ATC spheroids in *BRAF*
988 V600E–mutant in the 8505C and SW1736 cell lines. (T) The effect of treatment with BX795 (2.5
989 μM), Dab (2.5 μM), or their combination on patient-derived ATC spheroids (ATC01 and ATC02).

990 All data are presented as the mean ± standard deviation. Statistical significance is indicated as ns
991 = nonsignificant; *p < 0.05; **p < 0.01; ***p < 0.001; ****p < 0.0001.
992
993 **Fig. 2: Effect of combination BX795 and dabrafenib (Dab) treatment in an orthotopic ATC**
994 ***in vivo* model.**
995 Mice were treated with BX795 (100 mg/kg), Dab (15 mg/kg), or their combination 5 days per
996 week. After 2 weeks, tumors were excised and their volume (mm^3) (A) and weight (B) were
997 measured. (C–D) *In vivo* tumor growth was analyzed by tumor luminescence analysis (photons/s)
998 (C), and the fold change of each tumor was determined relative to the luminescence intensity of
999 the tumor site at day 0 (D). Comparisons were made across treatment groups at days 0, 7, and 14.
1000 (E) Body weight of mice on day 14 of the study. All data are presented as mean ± standard error
1001 of the mean. Statistical significance is indicated as ns = nonsignificant; *p < 0.05; **p < 0.01;
1002 ***p < 0.001.
1003
1004 **Fig. 3: Combined PDPK1 and BRAF V600E inhibition induces apoptosis and DNA damage**
1005 **in *BRAF* V600E–mutant anaplastic thyroid cancer (ATC).**
1006 (A) Mutated *BRAF* V600E ATC cells (8505C) were treated for 48 h with BX795 (2.5 μM),
1007 dabrafenib (Dab) (2.5 μM), or their combination. Then, total and phosphorylated protein levels
1008 were measured using mass spectrometry. (A–C) The volcano plots show significantly upregulated
1009 proteins in red, significantly downregulated proteins in blue ($p < 0.05$), and non-significant
1010 proteins in gray. The x-axis represents $\log_2$ fold change, and the y-axis shows $-\log_{10}$(p-value). The
1011 dashed lines indicate thresholds for statistical significance and fold change. (D) The Venn
1012 diagrams shows shared and treatment-specific differentially expressed proteins and
1013 phosphorylated proteins across the treatment groups ($p < 0.05$). The overlapping regions represent
1014 a conserved core proteomic response, while the non-overlapping regions indicate pathway-specific
1015 effects of PDPK1 or BRAF inhibition. (E–G) Gene set enrichment analysis (GSEA) of ranked
1016 phosphorylated site changes following BX795 (E), Dab (F), or combination (G) treatment. The
1017 bar plots show normalized enrichment scores (NES) for Hallmark Kyoto Encyclopedia of Genes
1018 and Genomes (KEGG) signaling pathways. (H) Western blot analysis of the effect of BX795 (2.5
1019 μM), Dab (2.5 μM), or combination treatment on *BRAF* V600E–mutant ATC cell lines (8505C
1020 and SW1736) after 48 h. pMEK, total MEK, $pAKT^{308}$, total AKT, $pPDPK1^{S241}$, PARP-1, BCL2,

1021 and caspase-3 protein levels are shown, with β-actin used as a loading control. (I) Flow cytometry
1022 results of Annexin V/PI staining with BX795 (2.5 μM), Dab (2.5 μM), or combination treatment.
1023 (J) Western blot analysis of apoptosis regulatory proteins 40 h after treatment. $pBAD^{S112}$, BAD,
1024 BCL2, $pGSK3\beta^{Ser9}$, GSK3β, and the double-stranded DNA damage marker $pH2AX^{S139}$ are shown,
1025 with β-actin used as a loading control. Protein band density was measured and normalized to β-
1026 actin. The phosphorylated to total protein ratios were measured, and the values are listed above
1027 the phosphoprotein band. Protein band density of BCL-xL and $pH2AX^{S139}$ were also measured and
1028 normalized to β-actin. (K) Immunoprecipitation of BCL-xL and BCL2 with BAD 30 h after
1029 treatment with BX795 and Dab in *BRAF* V600E–mutant ATC cell lines. Protein band density was
1030 measured and normalized to the input protein band. The ratio of immunoprecipitated to total input
1031 protein was measured and is listed below the protein blot. P = phosphorylation. The superscript
1032 indicates the amino acid phosphorylation site. (L) The heatmap shows z-scored log_2-transformed
1033 abundance of apoptosis-related proteins for the BX795, Dab, and combination treatment groups in
1034 8505C ATC cells. The proteins are displayed in sequential order—BAD, TNFRSF10A, PARP1,
1035 FAS, BID, CASP3, CASP8, BAX, CASP9, CASP7, BCL2L1, and BAK1—with hierarchical
1036 clustering applied to the rows. (M) The effect of BX795 (2.5 μM), Dab (2.5 μM), or combination
1037 treatment for 16 h on γH2AX foci formation in the 8505C and SW1736 ATC cell lines using
1038 immunofluorescence. γH2AX was labelled with Alexa Fluor™ 546 secondary antibody, with
1039 DAPI used for nuclear staining. A Zeiss LSM 800 confocal microscope was used to examine the
1040 cells (400× magnification). The number of foci per cell was quantified using ImageJ. All data are
1041 presented as the mean ± standard error of the mean of 25 cells. Statistical significance is indicated
1042 as ns = nonsignificant; *$p < 0.05$; **$p < 0.01$; ***$p<0.001$; ****$p < 0.0001$. (N) Western blot
1043 analysis of the effect of BX795 (2.5 μM), Dab (2.5 μM), or combination treatment for 16 h on
1044 DNA damage–dependent proteins (pATM, total ATM, pCHK2, Total CHK2, and pCHK1). β-
1045 Actin was used as a loading control. (O) Cell cycle analysis after BX795 (2.5 μM), Dab (2.5 μM),
1046 or combination treatment for 16 h in *BRAF* V600E–mutant ATC cell lines (8505C and SW1736).
1047 Cells were stained with propidium iodide (PI) and analyzed by fluorescence-activated cell sorting.
1048 The DNA content was measured, 2N (diploid) and 4N (tetraploid), based on the PI-stained DNA
1049 content. (P) The effect of BX795 (2.5 μM), Dab (2.5 μM), or combination treatment for 16 h on
1050 DNA repair proteins—cyclin D, cyclin B, pcdc25c, pCDK1, total CDK1, pH3A, H3A, and cyclin
1051 A2—by immunoblotting. β-actin was used as a loading control. The ratio of phospho-H3A to total
1052 H3A was measured and is listed below the phospho-H3A protein band. All data are presented as

1053 the mean ± standard deviation. Statistical significance is indicated as ns = nonsignificant; *p <
1054 0.05; **p < 0.01; ***p < 0.001; ****p < 0.0001. (Q) Analysis of the effect of combination BX795
1055 (2.5 μM) and Dab (2.5 μM) treatment for 16 h followed by proteasomal degradation inhibition for
1056 6 h (MG132, 10 μM). Protein band density was measured and normalized to β-actin. (R) The
1057 heatmap shows z-scored log2-transformed phosphorylation levels of DNA damage response, DNA
1058 repair, and cell-cycle regulatory proteins for the BX795, Dab, and combination treatment groups
1059 in 8505C ATC cell line. Proteins are displayed in sequential order as RAD50, CDK1, MCM2,
1060 PRKDC, RB1, TP53BP1, TP53, XRCC1, XRCC5, LIG1, MDC1, and MSH6, with supervised
1061 hierarchical clustering applied to the rows. The color scale represents relative protein levels (red
1062 = higher; blue = lower).
1063
1064 **Fig. 4: The effects of BX795 and dabrafenib (Dab) treatment on reactive oxygen species**
1065 **(ROS), mitochondrial function, and bioenergetics in *BRAF* V600E–mutant anaplastic**
1066 **thyroid cancer (ATC) cell lines.**
1067 Mutated BRAF V600E cell were treated with BX795 (2.5 μM), Dab (2.5 μM), or their
1068 combination. (A) Total cellular ROS was measured using the DCFH-DA fluorescent dye and
1069 quantified with flow cytometry. (B) Mitochondrial superoxide was measured based on MitoSOX
1070 red fluorescence, quantified with flow cytometry. (C–D) The mitochondrial content was assessed
1071 by MitoTracker green fluorescence, as quantified by flow cytometry and visualized with live-cell
1072 confocal microscopy (Zeiss LSM 800, 400× magnification). (E) The mitochondrial membrane
1073 potential was evaluated by TMRM (100 nM) fluorescence and analyzed by flow cytometry. (F)
1074 The oxygen consumption rate (OCR) was measured using a Seahorse analyzer with sequential
1075 injections of oligomycin (Oligo), 2,4-dinitrophenol (DNP), and antimycin A plus rotenone
1076 (Rot+AA). The data were normalized to the total protein content, and maximal respiration and
1077 adenosine triphosphate (ATP)-linked respiration were quantified accordingly. (G) The heatmap
1078 shows z-scored $\log_2$-transformed abundance of proteins associated with mitochondrial oxidative
1079 phosphorylation, the tricarboxylic acid (TCA) cycle, mitochondrial ribosomal, transport, and
1080 mitochondrial dynamics–associated proteins in 8505C ATC cells treated with BX795 (2.5 μM),
1081 Dab (2.5 μM), or their combination. The proteins include representatives of electron transport
1082 chain complexes I–V (NDUF subunits, SDHA–D, UQCRC1/2, COX subunits, and ATP5
1083 subunits), TCA cycle enzymes (IDH1, IDH2, IDH3, FH, OGDH, DLST, CS, MDH2, and
1084 PDHA1/PDHB), mitochondrial transport and structure (TOMM20, TIMM23, VDAC1–3, MFN1,

1085 OPA1, DNM1L), and mitochondrial genome maintenance (TFAM). Hierarchical clustering was
1086 applied to the rows. The color scale represents relative protein abundance (red = higher; blue =
1087 lower). All data are expressed as the mean ± standard deviation. Statistical significance is indicated
1088 as ns = nonsignificant; *p < 0.05; **p < 0.01; ***p < 0.001; ****p < 0.0001.
1089
1090 **Fig. 5: Reactive oxygen species (ROS) scavenging attenuates combination BX795 and**
1091 **dabrafenib (Dab) treatment effect while CHK2 inhibition leads to mitotic slippage and**
1092 **partial apoptotic reversal.**
1093 (A) Time-dependent effect of combination BX795 and Dab treatment based on propidium iodide
1094 (PI) staining, showing the proportion of cells arrested in the G2/M phase. Cells were stained with
1095 PI and analyzed by fluorescence-activated cell sorting. The results are presented as the mean ±
1096 standard deviation. Statistical significance is indicated as ns = nonsignificant; *p < 0.05; **p <
1097 0.01; ***p < 0.001; ****p < 0.0001. (B) Intracellular ROS levels were measured using DCFH-
1098 DA staining and analyzed by flow cytometry. The results are presented as the mean ± standard
1099 deviation. (C–E) The effects of *N*-acetyl cysteine (NAC) (5 mM) on combination treatment–
1100 induced responses in *BRAF* V600E–mutant ATC cell lines. (C) ROS generation was analyzed by
1101 DCFH-DA staining and is presented as the mean ± standard deviation. (D) Apoptosis was assessed
1102 based on Annexin V/PI staining. (E) Immunoblot analysis of PARP-1 cleavage using β-actin as a
1103 loading control. The densitometric quantification of cleaved vs pro-PARP cleavage in relation to
1104 loading control is shown below the bands. (F) The effect of the mitochondrial ROS scavenger
1105 MitoQ on combination treatment–induced G2/M arrest in *BRAF* V600E–mutant ATC cell lines.
1106 The DNA content was measured, 2N (diploid) and 4N (tetraploid), based on PI staining. The results
1107 are presented as the mean ± standard deviation. Statistical significance is indicated as ns =
1108 nonsignificant; *p < 0.05; **p < 0.01; ***p < 0.001; ****p < 0.0001. (G–H) The impact of CHK2
1109 phosphorylation inhibitor BML-277 (ML277) on combination BX795 and Dab treatment-induced.
1110 (G) Cell cycle arrest was analyzed by PI staining and flow cytometry. (H) Antiproliferative effect
1111 in *BRAF* V600E–mutant ATC cells. The DNA content was measured, 2N (diploid) and 4N
1112 (tetraploid), based on PI staining. The results are presented as the mean ± standard deviation.
1113 Statistical significance is indicated as ns = nonsignificant; *P < 0.05; **P < 0.01; ***P < 0.001;
1114 ****P < 0.0001. (I) Apoptosis was measured with Annexin V/PI staining and flow cytometry. The
1115 results are presented as mean ± standard deviation. Statistical significance is indicated as ns =
1116 nonsignificant; *p < 0.05; **p < 0.01; ***p < 0.001; ****p < 0.0001.

1117
1118 **Supplemental Figures**

1119 **Fig. S1: PDPK1 expression, the efficacy of PDPK1 inhibitors, and the effect of combination**
1120 **PDPK1 and BRAF V600E inhibition in anaplastic thyroid cancer (ATC) cells.**

1121 (A) The box-and-whisker plot shows the Chronos gene effect scores for PDPK1 across the top 10
1122 cancer lineages from the DepMap 25Q3 dataset. The scores represent the impact of PDPK1
1123 knockout on cell fitness, where more negative values indicate greater essentiality. Individual dots
1124 represent cell lines within each lineage, and boxes denote the median and interquartile range. The
1125 thyroid cancer lineage is highlighted in red. (B) PDPK1 messenger RNA (mRNA) expression
1126 presented as Expression $\log_2$(TPM+1) among different thyroid cancer cell lines: ATC, follicular
1127 thyroid cancer (FTC), well-differentiated thyroid cancer (WDTC), medullary thyroid cancer
1128 (MTC), and poorly differentiated thyroid cancer (PDTC). (C) The box-and-whicker plot shows the
1129 Chronos gene effect scores for PDPK1 across thyroid cancer subtypes from the DepMap 25Q3
1130 dataset. Individual data points represent cell lines, and boxes denote the median and interquartile
1131 range. ATC is highlighted in red. (D) Data from quantitative high-throughput drug screening in
1132 ATC cell lines (8505C, THJ16T, and THJ11T). Comparison of half-maximal inhibitory
1133 concentration (IC_{50}) < 10 μM and drug-response curve class of < 2.2 for known PDPK1 inhibitors
1134 (BX795, GSK2334470, OSU-03012, DTXSID90678515, and BX912) after treatment for 48 h. (E)
1135 PRISM drug sensitivity scores for BX795 (24Q2) across thyroid cancer subtypes, including
1136 WDTC, ATC, PDTC, and MTC. More negative values indicate greater sensitivity to BX795. The
1137 data are derived from pooled cell line responses within each subtype. (F) To analyze the effect of
1138 BX795 treatment, *BRAF* V600E–mutant ATC cell lines (8505C and SW1736) were treated with
1139 BX795 (2.5 or 5 μM) for 48 h, and then the levels of non-phosphorylated and phosphorylated
1140 mTOR, AKT (T^{308}), H_2AX (S^{15}), and S6K were evaluated by immunoblotting using β-actin as a

1141 loading control. (G) *BRAF* V600E–mutant ATC cell lines (8505C and SW1736) were transiently
1142 silenced with Control siRNA, PDPK1si1, or PDPK1si2 in combination with BX795 (2.5 μM) for
1143 48 h, and then the levels of phosphorylated PDPK1 (S^{245}), H_2AX, and PDPK1 were evaluated by
1144 immunoblotting using β-actin as a loading control. Their effect on cell proliferation was also
1145 measured. The results are presented as the mean ± SD. Statistical significance is indicated as ns =
1146 nonsignificant; *$p < 0.05$; **$p < 0.01$; ***$p < 0.001$; ****$p < 0.0001$. (H–I) Representative images
1147 of the colony-formation assay (H) and cellular migration (I) with BX795 and dabrafenib (Dab)
1148 treatment alone and their combination in *BRAF* V600E–mutant ATC cells. The representative
1149 images correspond to the data shown in Fig. 1K–N.
1150
1151 **Fig. S2: Combination BX795 and dabrafenib (Dab) treatment *in vivo*.**
1152 (A–B) Representative tumor images from all mouse groups at the end of the study by sex. (C–D)
1153 Analysis of the tumor weight (C) and tumor volume (D) at the study endpoint by sex. The results
1154 are presented as the mean ± standard error of the mean. Statistical significance is indicated as ns =
1155 nonsignificant; *$p < 0.05$.
1156
1157 **Fig. S3: Combination BX795 and dabrafenib (Dab) treatment induces apoptosis and G2**
1158 **arrest.**
1159 (A) The effect of treatment with BX795 (2.5 μM), Dab (2.5 μM), or their combination for 40 h
1160 on BCL2 and phospho-PDPK1 (pPDPK1) protein levels in *BRAF* V600E–mutant ATC cells
1161 (8505C). Immunofluorescence was performed with BCL2 labeled using Alexa Fluor™ 633
1162 secondary antibody and pPDPK1 labeled with Alexa Fluor™ 546 secondary antibody; DAPI was
1163 used as a nuclear counterstain. Images were acquired using a Zeiss LSM 800 confocal microscope

1164 at 400× magnification. (B) Densitometry results for the proteins shown in Fig. 4P, normalized to
1165 β-actin. The y-axis is the fold change relative to the control.
1166
1167 **Fig. S4: The effect of combination BX795 and dabrafenib (Dab) treatment on basal**
1168 **respiration, the mitochondrial membrane potential, DNA damage proteins, and cell cycle**
1169 **arrest.**
1170 (A) Analysis of the effect of treatment with BX795, Dab, or their combination on basal respiration
1171 in *BRAF* V600E–mutant ATC cell lines (8505C and SW1736), measured with the Seahorse assay.
1172 The basal respiration rate was normalized to the total protein content and is presented as the mean
1173 ± standard deviation. (B) Mitochondrial integrity was assessed by JC-1 staining after combination
1174 treatment, with the red-to-green fluorescence ratio determined with flow cytometry. The results
1175 are presented as mean ± standard deviation. (C) Immunoblot analysis of oxidative phosphorylation
1176 proteins following treatments, using β-actin as a loading control. Protein band density was
1177 determined and normalized to β-actin. The y-axis is the fold change relative to the control
1178 (DMSO). (D–E) Time-dependent effects (0–40 h) of treatment with BX795 (2.5 μM), Dab (2.5
1179 μM), or their combination on the mitochondrial membrane potential (D) and mitochondrial content
1180 (E) in *BRAF* V600E–mutant ATC cell lines. The mitochondrial membrane potential was assessed
1181 using TMRM (100 nM) fluorescence, and the mitochondrial content was measured with
1182 MitoTracker Green dye, with flow cytometry used for quantification. The data are presented as the
1183 mean ± standard deviation. (F) Immunoblot analysis of phosphorylated CHK2 (pCHK2),
1184 phosphorylated ATM (pATM), and phosphorylated H2AX (pH2AX) levels in *BRAF* V600E–
1185 mutant ATC cell lines treated with BX795 (2.5 μM) and Dab (2.5 μM) in the presence or absence
1186 of *N*-acetyl cysteine (NAC) (5 mM). β-Actin was used as a loading control. (G) Representative
1187 results of Fig. 5G. (H–I) Analysis of the effect of the AZD7762 on cell cycle arrest and the

antiproliferative effect induced by combination BX795 and Dab treatment in *BRAF* V600E–mutant ATC cells (SW1736). The results are presented as the mean ± standard deviation. Statistical significance is indicated as ns = nonsignificant; *$p < 0.05$; **$p < 0.01$; ***$p < 0.001$; ****$p < 0.0001$.

Fig. 1a

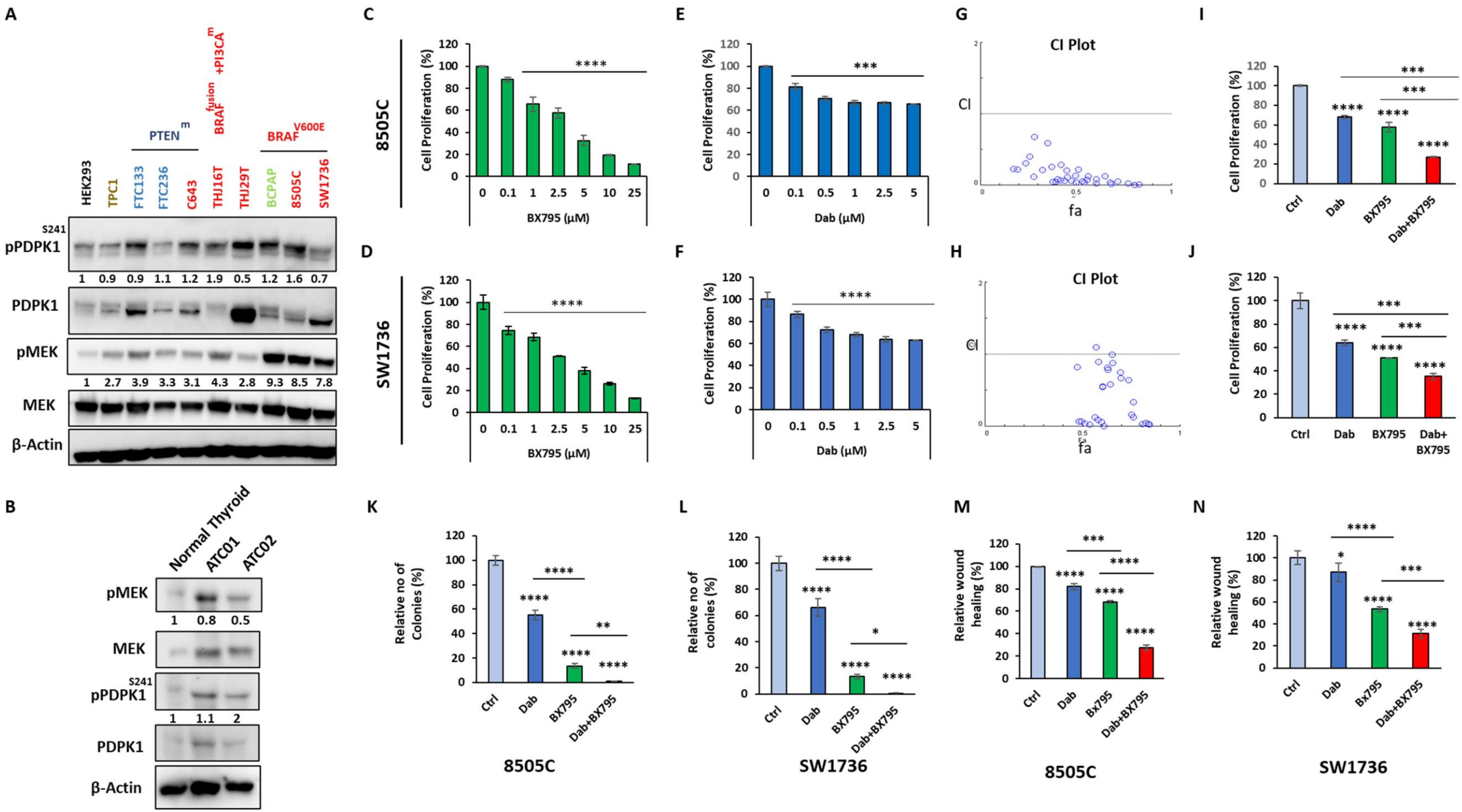
A
HEK293
TPC1
FTC133
FTC236
C643
THJ16T
THJ29T
BCPAP
8505C
SW1736
PTEN m
BRAF fusion +PI3CA m
BRAF V600E
S241
pPDPK1
1 0.9 0.9 1.1 1.2 1.9 0.5 1.2 1.6 0.7
PDPK1
pMEK
1 2.7 3.9 3.3 3.1 4.3 2.8 9.3 8.5 7.8
MEK
β-Actin
B
Normal Thyroid
ATC01
ATC02
pMEK
1 0.8 0.5
MEK
S241
pPDPK1
1 1.1 2
PDPK1
β-Actin
C
8505C
Cell Proliferation (%)
BX795 (μM)
D
SW1736
E
Dab (μM)
F
G
CI Plot
CI
fa
H
I
Ctrl
Dab
BX795
Dab+BX795
J
Dab+ BX795
K
Relative no of Colonies (%)
L
Relative no of colonies (%)
M
Relative wound healing (%)
N

Fig. 1b

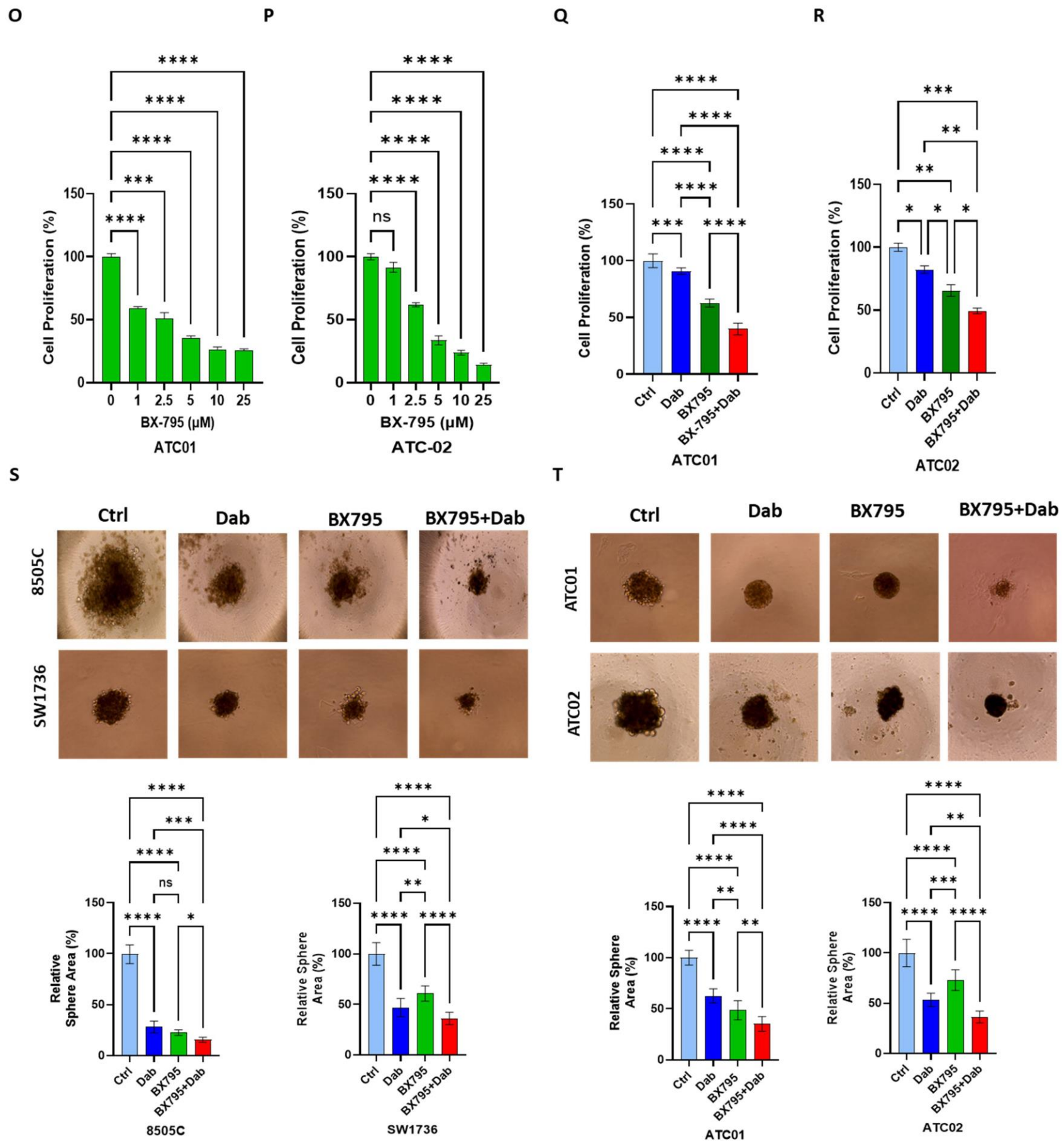
O
P
Q
R
Cell Proliferation (%)
BX-795 (μM)
ATC01
ATC-02
Ctrl
Dab
BX795
BX-795+Dab
BX795+Dab
ATC02
S
T
8505C
SW1736
Relative Sphere Area (%)

Fig. 2

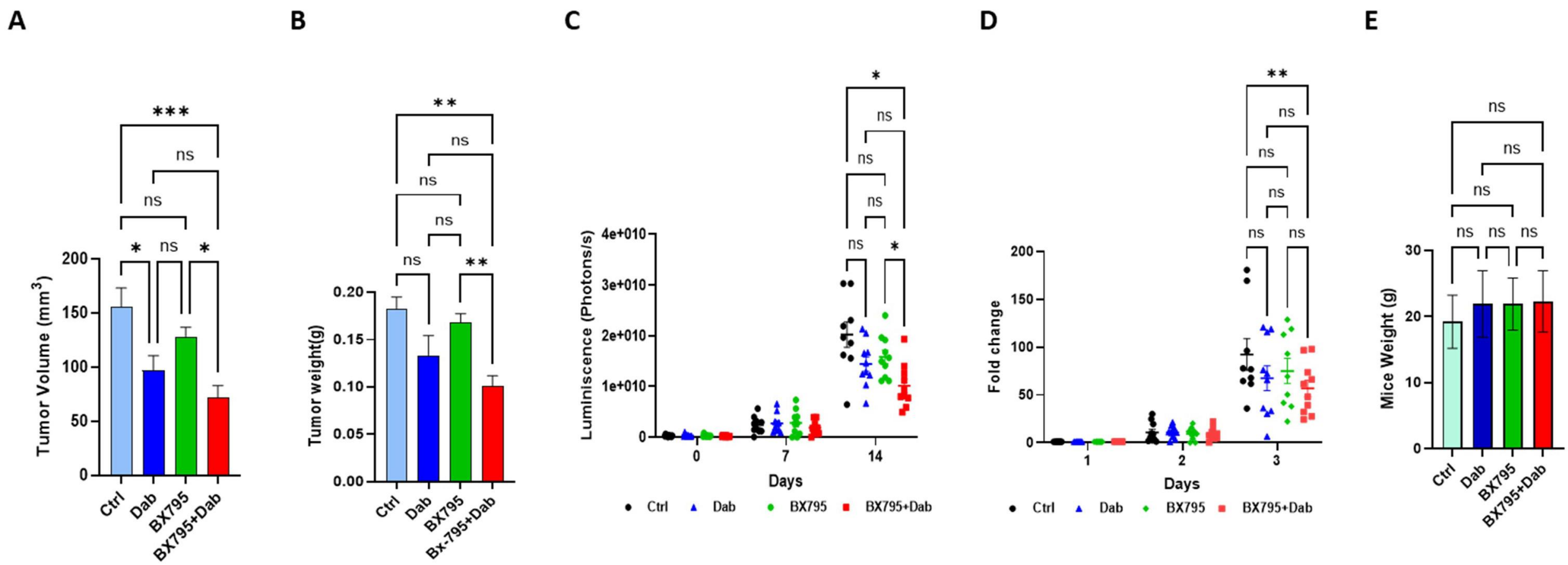
A
B
C
D
E
Tumor Volume (mm3)
Tumor weight(g)
Luminiscence (Photons/s)
Fold change
Mice Weight (g)
Days
Ctrl
Dab
BX795
BX795+Dab
Bx-795+Dab
ns
*
**
***

Fig. 3a

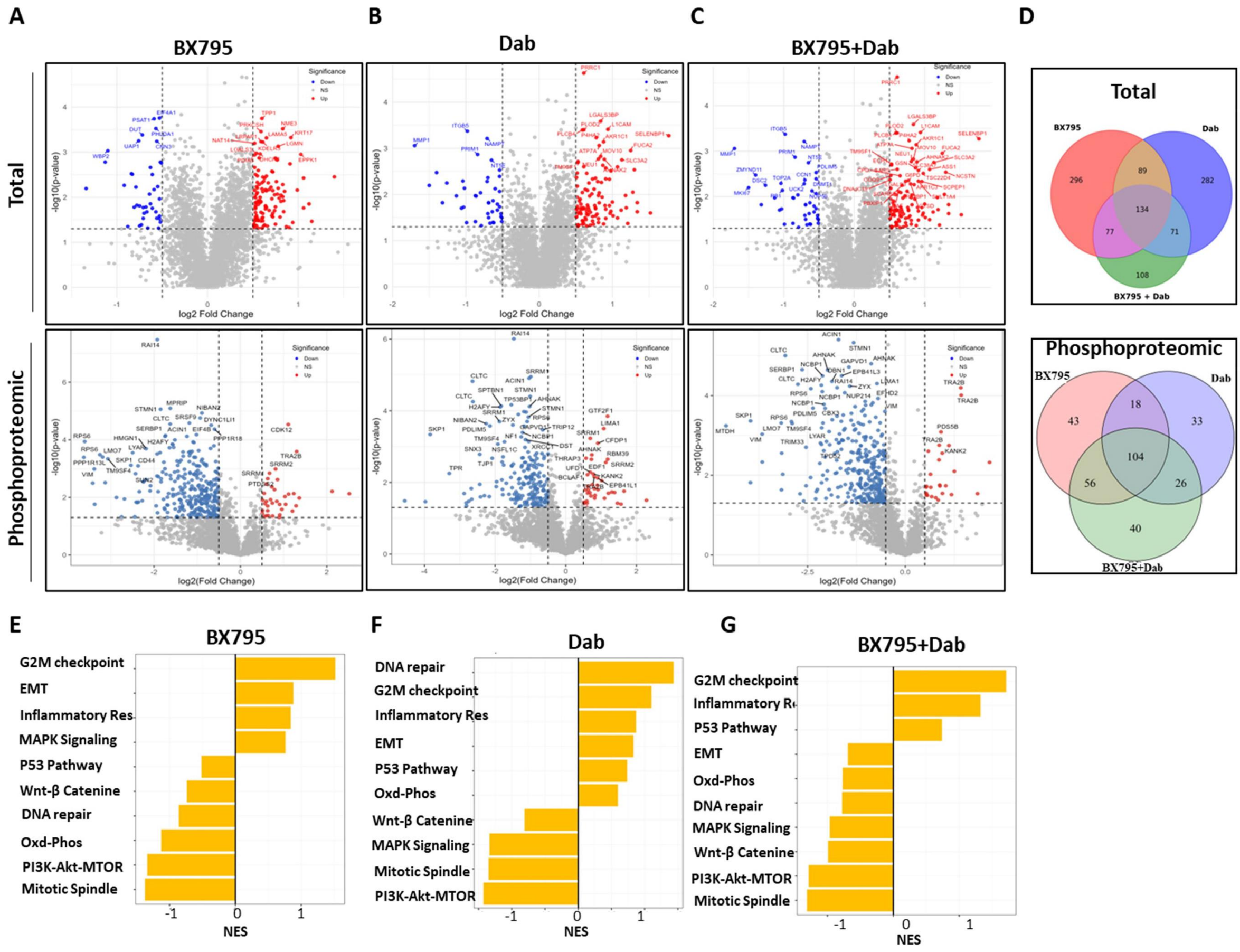
A
B
C
D
BX795
Dab
BX795+Dab
Total
Phosphoproteomic
Significance
Down
NS
Up
-log10(p-value)
log2 Fold Change
log2(Fold Change)
Total
BX795
Dab
BX795 + Dab
296
89
282
134
77
71
108
Phosphoproteomic
BX795
Dab
BX795+Dab
43
18
33
104
56
26
40
E
F
G
BX795
Dab
BX795+Dab
G2M checkpoint
EMT
Inflammatory Res
MAPK Signaling
P53 Pathway
Wnt-β Catenine
DNA repair
Oxd-Phos
PI3K-Akt-MTOR
Mitotic Spindle
NES

Fig. 3b

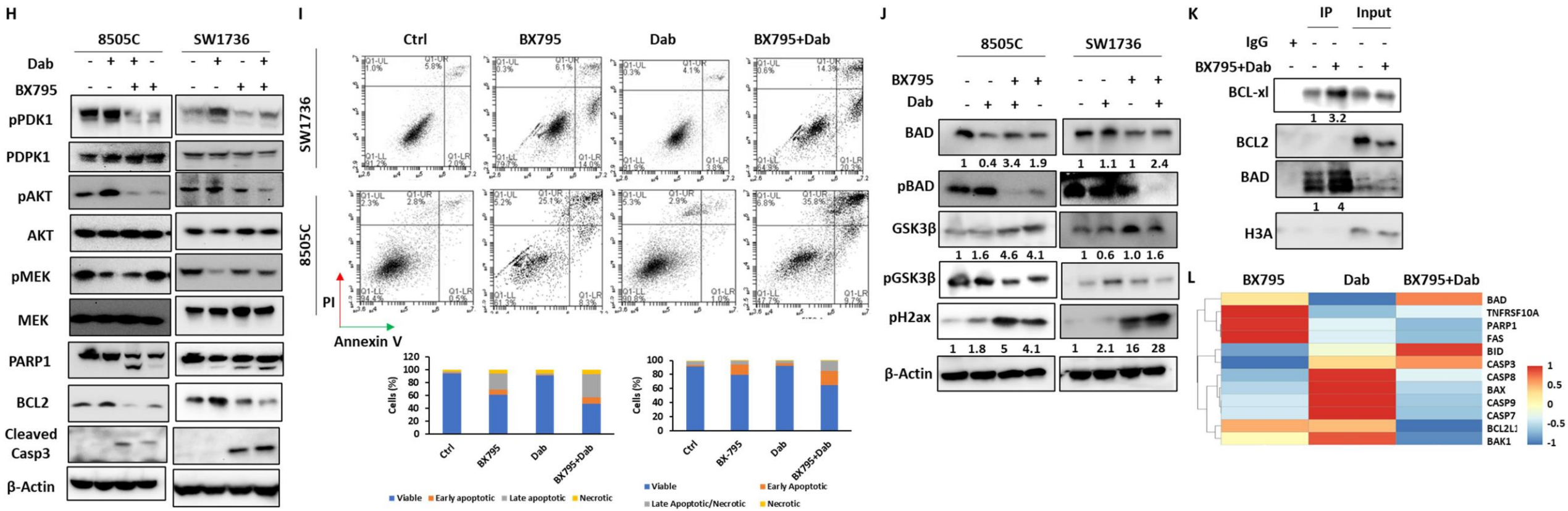
H
8505C
SW1736
Dab
BX795
pPDK1
PDPK1
pAKT
AKT
pMEK
MEK
PARP1
BCL2
Cleaved Casp3
β-Actin
I
Ctrl
BX795
Dab
BX795+Dab
SW1736
8505C
PI
Annexin V
Cells (%)
Viable
Early apoptotic
Late apoptotic
Necrotic
Early Apoptotic
Late Apoptotic/Necrotic
J
BAD
pBAD
GSK3β
pGSK3β
pH2ax
β-Actin
K
IP
Input
IgG
BCL-xl
BCL2
BAD
H3A
L
BAD
TNFRSF10A
PARP1
FAS
BID
CASP3
CASP8
BAX
CASP9
CASP7
BCL2L1
BAK1

Fig. 3c

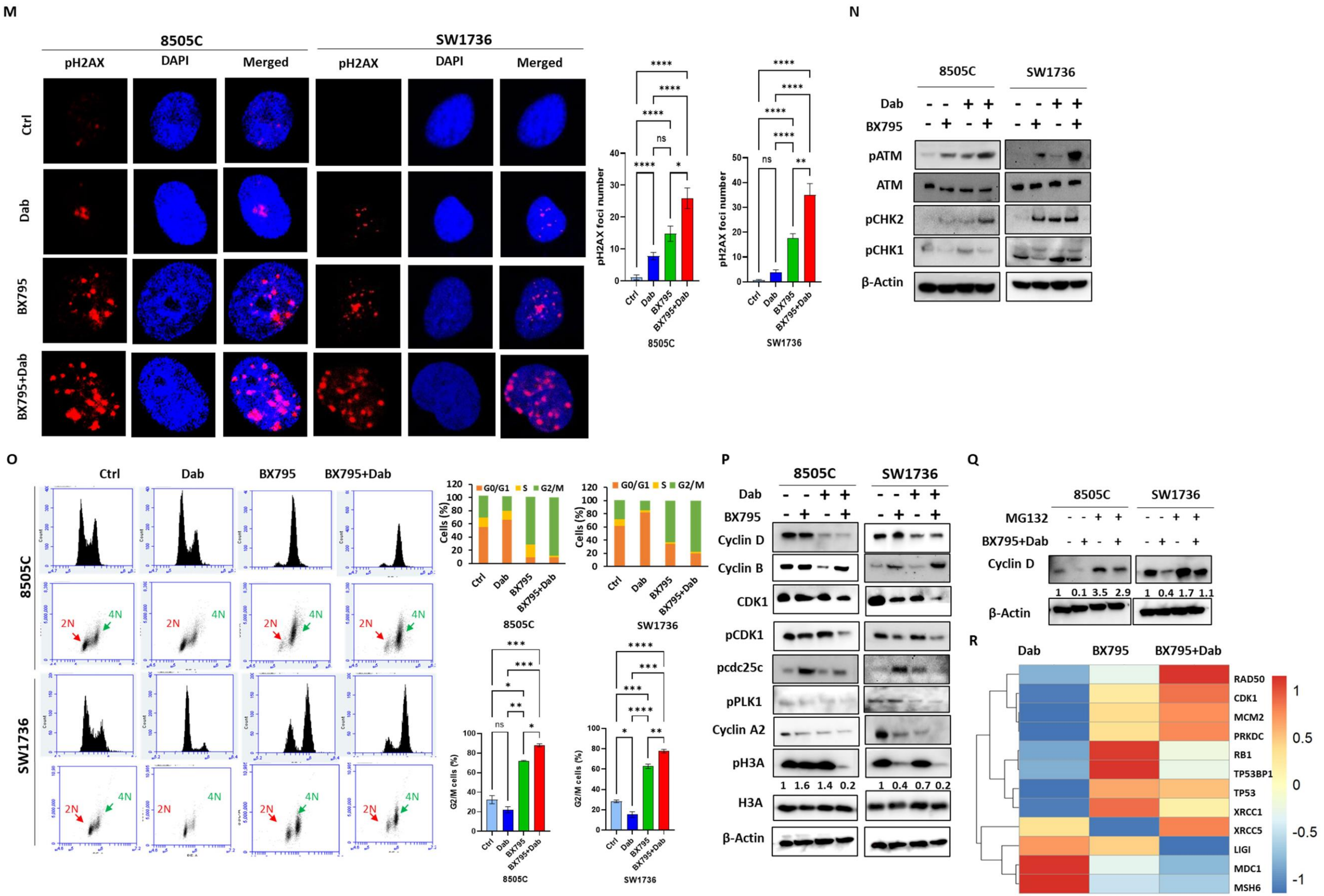
M
8505C
SW1736
pH2AX
DAPI
Merged
Ctrl
Dab
BX795
BX795+Dab
pH2AX foci number
Ctrl
Dab
BX795
BX795+Dab
8505C
SW1736
N
8505C
SW1736
Dab
BX795
pATM
ATM
pCHK2
pCHK1
β-Actin
O
Ctrl
Dab
BX795
BX795+Dab
8505C
SW1736
2N
4N
G0/G1
S
G2/M
Cells (%)
G2/M cells (%)
P
8505C
SW1736
Dab
BX795
Cyclin D
Cyclin B
CDK1
pCDK1
pcdc25c
pPLK1
Cyclin A2
pH3A
1 1.6 1.4 0.2
1 0.4 0.7 0.2
H3A
β-Actin
Q
8505C
SW1736
MG132
BX795+Dab
Cyclin D
1 0.1 3.5 2.9
1 0.4 1.7 1.1
β-Actin
R
Dab
BX795
BX795+Dab
RAD50
CDK1
MCM2
PRKDC
RB1
TP53BP1
TP53
XRCC1
XRCC5
LIGI
MDC1
MSH6
1
0.5
0
-0.5
-1

Fig. 4

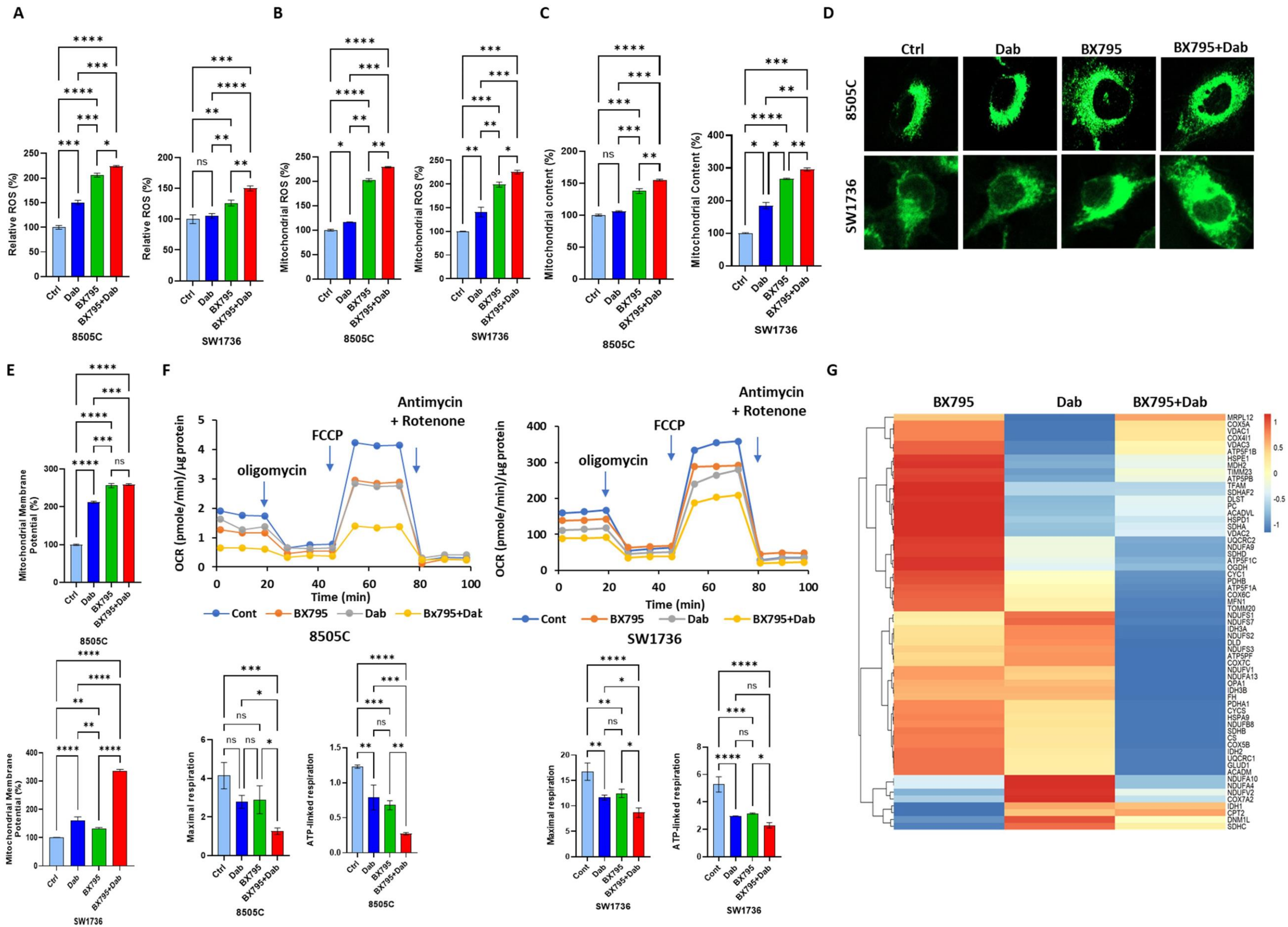
A
Relative ROS (%)
Ctrl
Dab
BX795
BX795+Dab
8505C
SW1736
B
Mitochondrial ROS (%)
C
Mitochondrial content (%)
Mitochondrial Content (%)
D
Ctrl
Dab
BX795
BX795+Dab
8505C
SW1736
E
Mitochondrial Membrane Potential (%)
F
Antimycin + Rotenone
FCCP
oligomycin
OCR (pmole/min)/µg protein
Time (min)
Cont
BX795
Dab
Bx795+Dab
BX795+Dab
Maximal respiration
ATP-linked respiration
G
BX795
Dab
BX795+Dab
MRPL12
COX5A
VDAC1
COX4I1
VDAC3
ATP5F1B
HSPE1
MDH2
TIMM23
ATP5PB
TFAM
SDHAF2
DLST
PC
ACADVL
HSPD1
SDHA
VDAC2
UQCRC2
NDUFA9
SDHD
ATP5F1C
OGDH
CYC1
PDHB
ATP5F1A
COX6C
MFN1
TOMM20
NDUFS1
NDUFS7
IDH3A
NDUFS2
DLD
NDUFS3
ATP5PF
COX7C
NDUFV1
NDUFA13
OPA1
IDH3B
FH
PDHA1
CYCS
HSPA9
NDUFB8
SDHB
CS
COX5B
IDH2
UQCRC1
GLUD1
ACADM
NDUFA10
NDUFA4
NDUFV2
COX7A2
IDH1
CPT2
DNM1L
SDHC

Fig. 5a

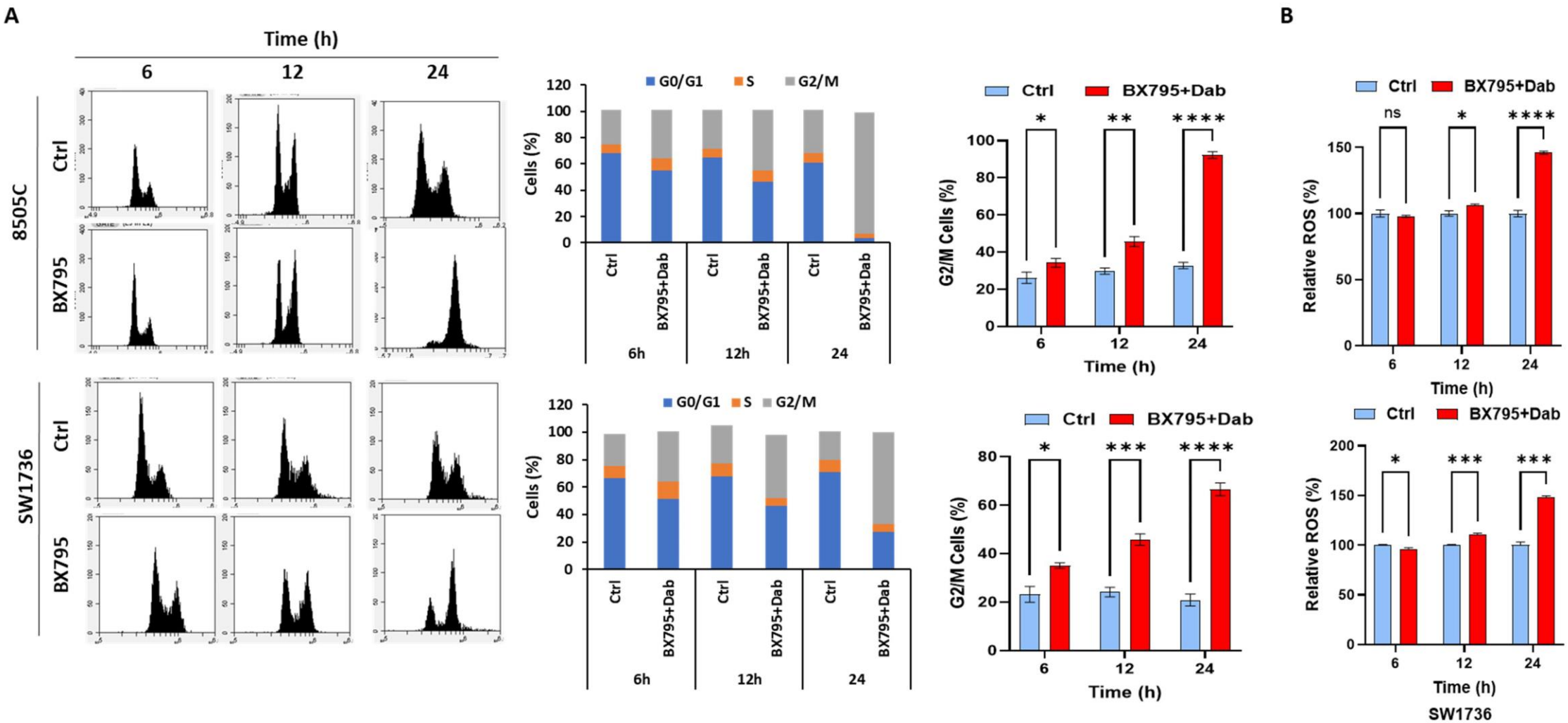
A
Time (h)
6
12
24
8505C
Ctrl
BX795
SW1736
Ctrl
BX795
G0/G1
S
G2/M
Cells (%)
Ctrl
BX795+Dab
6h
12h
24
G2/M Cells (%)
Time (h)
B
Relative ROS (%)
ns
SW1736

Fig. 5b

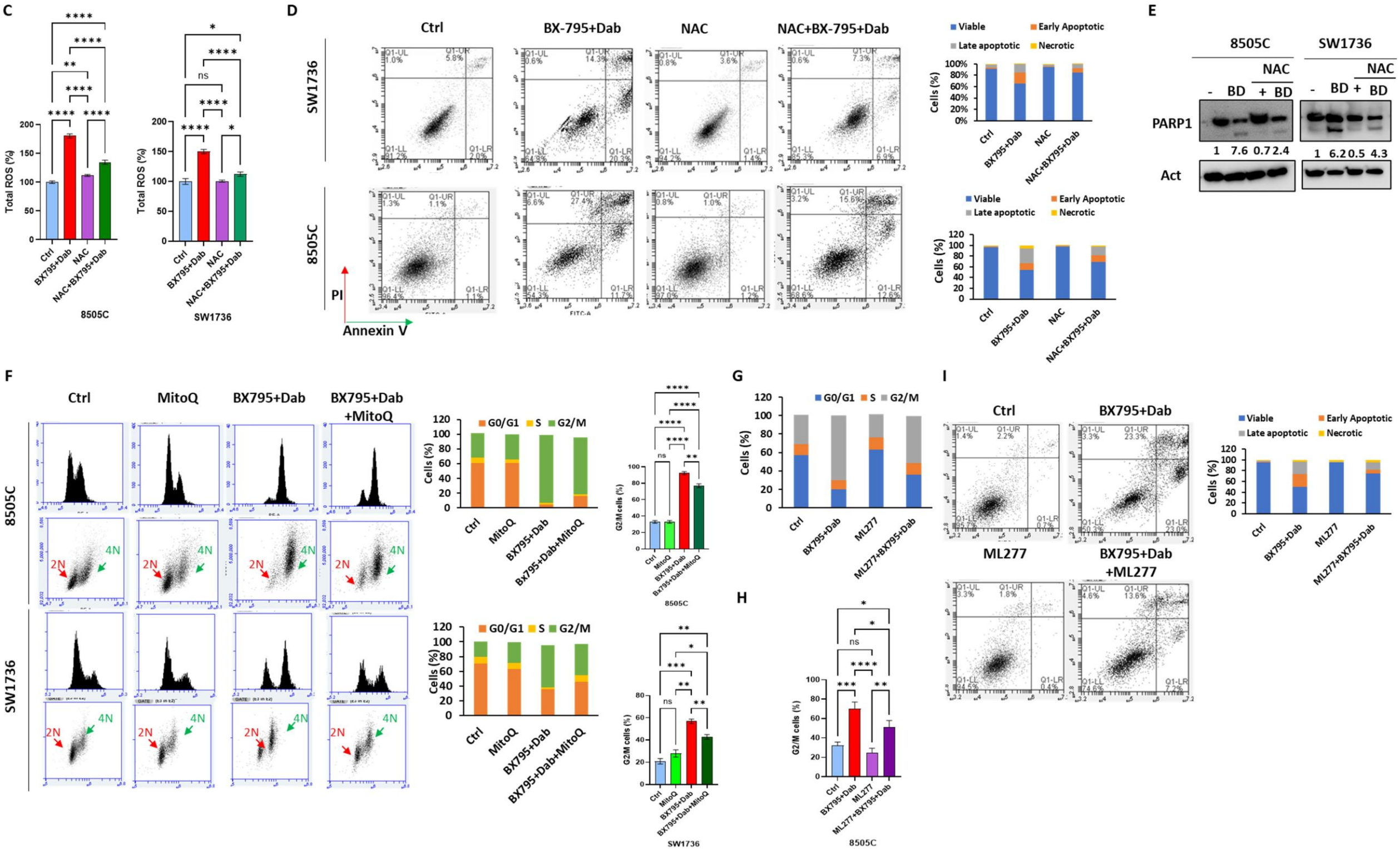
C
Total ROS (%)
Ctrl
BX795+Dab
NAC
NAC+BX795+Dab
8505C
SW1736
D
Ctrl
BX-795+Dab
NAC
NAC+BX-795+Dab
SW1736
8505C
PI
Annexin V
Viable
Early Apoptotic
Late apoptotic
Necrotic
Cells (%)
E
8505C
SW1736
NAC
BD
PARP1
Act
F
Ctrl
MitoQ
BX795+Dab
BX795+Dab +MitoQ
8505C
SW1736
2N
4N
G0/G1
S
G2/M
Cells (%)
G2/M cells (%)
G
ML277
ML277+BX795+Dab
H
I
BX795+Dab +ML277